

A novel mitochondrial metabolism-related gene signature for predicting the prognosis of oesophageal squamous cell carcinoma

Wenhao Lin^{1,2,*}, Changchun Ye^{2,*}, Liangzhang Sun¹, Zilu Chen², Chao Qu², Minxia Zhu^{1,3}, Jianzhong Li¹, Ranran Kong¹, Zhengshui Xu^{1,4}

¹Department of Thoracic Surgery, The Second Affiliated Hospital of Xi'an Jiaotong University, Xi'an 710004, Shaanxi, China

²Department of General Surgery, The First Affiliated Hospital of Xi'an Jiaotong University, Xi'an 710061, Shaanxi, China

³Department of Thoracic Surgery, The First Affiliated Hospital of Wenzhou Medical University, Wenzhou 325000, Zhejiang, China

⁴Key Laboratory of Surgery Critical Care and Life Support (Xi'an Jiaotong University), Ministry of Education, Xi'an 710061, Shaanxi, China

*Equal contribution

Correspondence to: Zhengshui Xu; email: xuzhengshui@xjtu.edu.cn

Keywords: mitochondrial metabolism, oesophageal squamous cell carcinoma, prognosis, nomogram

Received: October 27, 2023

Accepted: May 3, 2024

Published: June 5, 2024

Copyright: © 2024 Lin et al. This is an open access article distributed under the terms of the [Creative Commons Attribution License](https://creativecommons.org/licenses/by/4.0/) (CC BY 4.0), which permits unrestricted use, distribution, and reproduction in any medium, provided the original author and source are credited.

ABSTRACT

Oesophageal squamous cell carcinoma (ESCC) is one of the most lethal cancers worldwide. Due to the important role of mitochondrial metabolism in cancer progression, a clinical prognostic model based on mitochondrial metabolism and clinical features was constructed in this study to predict the prognosis of ESCC. Firstly, the mitochondrial metabolism scores (MMs) were calculated based on 152 mitochondrial metabolism-related genes (MMRGs) by single sample gene set enrichment analysis (ssGSEA). Subsequently, univariate Cox regression and LASSO algorithm were used to identify prognosis-associated MMRG and risk-stratify patients. Functional enrichment, interaction network and immune-related analyses were performed to explore the features differences in patients at different risks. Finally, a prognostic nomogram incorporating clinical factors was constructed to assess the prognosis of ESCC. Our results found there were differences in clinical features between the MMs-high group and the MMs-low group in the TCGA-ESCC dataset ($P < 0.05$). Afterwards, we identified 6 MMRGs (COX10, ACADVL, IDH3B, AKR1A1, LIAS, and NDUFB8) signature that could accurately distinguish high-risk and low-risk ESCC patients. A predictive nomogram that combined the 6 MMRGs with sex and N stage to predict the prognosis of ESCC was constructed, and the areas under the receiver operating characteristic (ROC) curve at 1, 2 and 3 years were 0.948, 0.927 and 0.848, respectively. Finally, we found that COX10, one of 6 MMRGs, could inhibit the malignant progression of ESCC *in vitro*. In summary, we constructed a clinical prognosis model based on 6 MMRGs and clinical features which can accurately predict the prognosis of ESCC patients.

INTRODUCTION

Oesophageal squamous cell carcinoma (ESCC) is the predominant histological type of oesophageal cancer worldwide [1], accounting for approximately 85% of

oesophageal cancer patients [2]. Although multimodality therapies, including surgery, chemotherapy, radiation therapy and molecular targeted therapy, are currently available for ESCC patients, the 5-year overall survival (OS) rate is still not satisfactory and remains in the range

of 10%–30% in most countries [2–4]. Therefore, it is very important to identify a prognosis-related gene signature for ESCC and establish a prediction model for the individualized treatment of ESCC patients in the context of precision medicine.

Mitochondria are the center of oxidative phosphorylation and adenosine triphosphate (ATP) biosynthesis; ATP provides the majority of energy for mammalian cell biological processes [5]. Mitochondria also had a vital influence on the progression of malignant tumours due to their special position in energy metabolism [6]. Defective mitochondrial translation has been implicated in pathologies such as ageing, metabolic syndromes, and cancer [7]. Mitochondrial and metabolic pathway disorders caused by mitochondrial metabolism-related genes (MMRGs) promote tumour development, progression, and immune evasion [8, 9]. Previous research showed that MMRGs are strongly correlated with the malignancy of multiple tumours, such as pancreatic cancer, hepatocellular carcinoma, and acute myeloid leukaemia [10–14]. In ESCC, genes located in the mitochondrial inner membrane, such as the interferon-stimulating gene IFI6, are significantly over-expressed, which is related to the invasive phenotype and poor prognosis [9]. However, there is not enough data to identify the genetic characteristics related to MMRGs in ESCC and explore their impact on patient prognosis.

In the present study, we systematically analysed the expression levels, mutations and biological function of the 152 MMRGs in ESCC. In addition, we confirmed the key MMRGs in ESCC, and a prognostic risk score model based on the MMRGs signature and clinical features was constructed; the model successfully identified patients with higher prognostic risk.

MATERIALS AND METHODS

Data collection and processing

The count data, transcripts per million (TPM), and clinical data of the ESCC dataset were obtained from The Cancer Genome Atlas (TCGA) [15]. In total, 70 ESCC cancer samples with survival data and a final set of 18063 genes were included. The “Masked Somatic Mutation” data served as somatic mutation data [16], and the “Masked Copy Number Segment” data served as copy number variation (CNA) data; these data were visualized by R software. Tumour mutation burden (TMB) and microsatellite instability (MSI) were collected from the cBioPortal for Cancer Genomics (<https://www.cbioportal.org/>) [17]. GSE20347 (T=17, N=17, T means tumour and N means normal tissue) [18], GSE161533 (T=28, N=28), and GSE23400 (T=53,

N=53) [19] were retrieved from the Gene Expression Omnibus (GEO) database [20] and merged to create a combined dataset for subsequent validation.

A total of 10 MMRGs were obtained from the GeneCards database [21] with relevance scores >2, and another 188 MMRGs were obtained from the KEGG PATHWAY database. Finally, 152 MMRGs were obtained by removing genes not found in the TCGA-ESCC dataset and the combined-dataset for subsequent analysis, as shown in Supplementary Table 1. All workflows are shown in Supplementary Figure 1.

Calculation of the mitochondrial metabolism scores (MMs)

MMs in the merged dataset were calculated by the GSVA package [21] through the single sample gene set enrichment analysis (ssGSEA) algorithm. Then, the TCGA-ESCC dataset was grouped by the median of MMs, and the difference between the MMs-high and MMs-low groups was visualized by an accumulation map.

Weighted gene co-expression network analysis (WGCNA)

The WGCNA package [22], with the settings of RsquaredCut to 0.85, the minimum number of module genes to 25, the module combined cutting height to 0, and the minimum distance to 0.2, was used to generate the co-expression module of TCGA-ESCC sample genes and MMs [11]. The R package clusterProfiler [23] was utilized to perform GO/KEGG [24, 25] analysis on the module genes with the largest positive and negative correlation, based on the standards of $P.adjust < 0.05$ and $FDR (Q.value) < 0.20$.

Recognition of MMRG molecular subtypes

The patient samples from the TCGA-ESCC dataset were classified with the R package ConsensusClusterPlus [26] according to the expression of MMRGs with unsupervised clustering. The number of clusters was set between 2 and 8, 1000 repeats were performed to extract 80% of the total samples, and clusterAlg= “pam” and distance= “euclidean” were run. Then, the infiltration of 28 tumour infiltration-associated immune cells was determined using the ssGSEA algorithm [27].

Construction of the prognosis model based on MMRGs

Univariate Cox regression analysis was performed to identify the MMRGs related to OS with genes exhibiting P -values < 0.1. Subsequently, the significant

variables were identified after eliminating multicollinearity through the LASSO algorithm. The risk score of each patient was calculated using the following formula.

$$\text{riskScore} = \sum_i \text{Coefficient}(\text{gene}_i) * \text{mRNA Expression}(\text{gene}_i)$$

Finally, the nomogram was constructed using R packet rms [28], and samples were divided into two groups based on the median risk score. To verify the stability and prediction ability of the model, decision curve analysis (DCA) [29], Kaplan-Meier (KM) curve and Receiver Operating Characteristic (ROC) curve were performed by R. The combined-dataset was used as a validation set for the same analysis as detailed above.

Functional similarity analysis

The differentially expressed genes (DEGs) between the high- and low-risk groups were obtained using the DESeq2 package ($P_{\text{adjust}} < 0.05$ and $|\log_{2}\text{FC}| > 1$). Then, GO/KEGG enrichment analysis for DEGs was performed. The GOSemSim package [30] was used to calculate the GO semantic similarity of genes, and the geometric mean of genes was calculated at the biological process (BP), cellular component (CC), and molecular function (MF) levels to obtain the final score. The ggplot package was used for visual analysis and visualization of the results.

Identification and enrichment analysis of differentially expressed MMRGs

Gene Set Enrichment Analysis (GSEA) [31] is often used to evaluate the contribution of gene sets to functional phenotypes. The DEGs of TCGA-ESCC were sorted according to $\log_{2}\text{FC}$ and were enriched through the clusterProfiler package. Then, GSEA was conducted utilizing the following parameters: the seed number was 2020, which was calculated 1000 times, and each gene set contained at least 10 genes, with a maximum of 500 genes. We obtained the “c2.cp.all.v2022.1.Hs.symbols.gmt [All Canonical Pathways](3050)” gene set from the MSigDB database [32]. The significantly enriched screening criteria were $P_{\text{adjust}} < 0.05$ and FDR value ($Q_{\text{value}} < 0.20$).

Construction of the interaction network

The prediction of functionally similar genes among the selected key genes and the construction of an interaction network were carried out using the GeneMANIA website [33]. The prediction of miRNAs that interact with the key genes was carried out using the miRDB

database [34], and an mRNA–miRNA interaction network was constructed for mRNAs with a target score > 80 using the miRDB database.

Immune infiltration and variation analysis

We evaluated the immune cell infiltration status in the high- and low-risk groups using CIBERSORT (<https://cibersort.stanford.edu/>) [35] and calculated the relationships between various immune cells. The correlation between the key genes and immune infiltrating cells was determined, and a heatmap was generated for visualization using the R package “ggplot2”.

The somatic mutation data were pre-processed using VarScan software, and somatic mutations in the high-risk group were visualized using the maftools package [16]. The masked copy number segment data were downloaded using the R package TCGAbiolinks, and then GISTIC 2.0 analysis was conducted [36] through the Hiplot website (<https://hiplot-academic.com/advance/gistic2>).

Construction of the clinical prognosis model

Based on TCGA-ESCC expression profile data, we used multivariate Cox regression, selected risk score combined with clinical features for Cox univariate analysis, and selected variable diseases with $P < 0.1$ to be included in the multivariate model. The predictive power of the model or a single variable was assessed by time-dependent ROC.

Immunohistochemistry (IHC) and immunofluorescence

For IHC and immunofluorescence, the staining procedure was performed using the standard avidin–biotin complex method. Two pathologists evaluated all the specimens in a blinded manner. Five ESCC tissue samples and their paraneoplastic tissues were randomly selected from ESCC patients who had not received radiotherapy or chemotherapy before excision between May 2023 and August 2023. All patients underwent surgery at the Second Affiliated Hospital of Xi'an Jiaotong University. Informed consent was obtained for all patients. The details of the antibodies are presented in Supplementary Table 2.

Cell culture and *in vitro* experiments

The KYSE140 (human oesophageal squamous cell carcinoma) cell line was maintained in RPMI-1640 medium supplemented with 10% FBS (Gibco BRL, Carlsbad, CA, USA) and 100 units/ml penicillin and streptomycin at 37° C in a humidified 5% CO₂

atmosphere. Lentiviral infection was performed according to the manufacturer's protocol as previously described [37]. The clone formation, migration and invasion assays were performed as previously described [38].

Statistical analysis

All data processing and analysis were performed using R software (Version 4.1.2). For the comparison of two groups of continuous variables, the statistical significance of normally distributed variables was estimated through independent Student's *t* test, and the difference between nonnormally distributed variables was analysed through the Wilcoxon rank-sum test. Comparisons with three or more groups were analysed using the Kruskal–Wallis test. The chi-square test or Fisher's exact test was employed to compare and analyse the statistical significance of differences between two groups of categorical variables. The threshold for statistical significance was $P < 0.05$. In this study, ns stands for $P \geq 0.05$, * for $P < 0.05$, ** for $P < 0.01$, *** for $P < 0.001$, and **** for $P < 0.0001$.

RESULTS

Mitochondrial metabolism scores and SNP/CNV analysis of MMRGs

To understand the relationship between ESCC and mitochondrial metabolism, we calculated MMs for the TCGA-ESCC cohort based on 152 MMRGs. Afterwards, we demonstrated the differences in various clinical features (age, sex, T stage, N stage, M stage, and stage) between the high and low MMs groups divided by median MMs (Supplementary Figure 2A–2F). In the MMs-high group, the percentage of N2 and N3 was higher than those in the MMs-low group. Then we identified the mutations in 152 MMRGs (Supplementary Figure 2G) and the mutation waterfall plot of MMRGs was generated (Supplementary Figure 2H), with HTT having the highest mutation frequency. Finally, we analysed the copy number variation among the 152 MMRGs in ESCC (Supplementary Figure 2I). Results showed that EHHADH and NDUF5 had the most copy number amplifications.

Weighted co-expression network analysis

To further identify the MMRGs closely related to ESCC, we conducted WGCNA on the TCGA-ESCC dataset to screen for co-expression modules. The analysis results showed that the optimal soft threshold was 9 (Figure 1A), and the genes in the TCGA-ESCC dataset were clustered into 16 modules (Figure 1B). Among them, METan had the highest positive correlation with MMs, with a correlation coefficient of

$R=0.41$, while MEblue had the highest negative correlation with MMs ($R=-0.55$). The gene lists for METan and MEblue are shown in Supplementary Table 3, and the clustering of the module is shown in Figure 1C. Then, we conducted GO/KEGG analyses on the two modules with the highest correlation with MMs in the TCGA-ESCC dataset to explore their potential biological mechanisms. The 169 METan module genes were enriched in BPs, such as multiple organic water homeostasis; CCs, such as apical part of cell and apical plasma membrane; and MFs, such as oxidoreductase activity and incorporation of one atom of oxygen (Figure 1D and Supplementary Table 4). The 858 MEblue module genes were enriched in BPs, such as extracellular matrix organization and extracellular structure organization; CCs, such as collagen-containing extracellular matrix; and MFs, such as ECM-receiver interaction and the PI3K-Akt signalling pathway (Figure 1E and Supplementary Table 5).

Unsupervised clustering of MMRGs

To better characterize the heterogeneity of mitochondrial metabolism in ESCC patients, we used the expression data of 152 MMRGs to perform unsupervised clustering of all ESCC patient samples based on a consensus clustering algorithm, which was used to identify the corresponding molecular subtypes. The results suggested that when the optimal number of clusters was 2, the cluster effect was the best (Figure 2A–2C). Therefore, we clustered all samples into two clusters (Cluster1=31 and Cluster2=39). Principal component analysis (PCA) showed that all patients were roughly divided into two groups, confirming the stability of this clustering (Figure 2D). To further validate the reliability of this clustering approach, we also included a merged dataset of the 3 GEO datasets as an external validation. The batch effects of the 3 datasets were removed in the merger (Supplementary Figure 3A–3D). We conducted the same analysis on the combined-dataset, and this dataset was also divided into two categories (Cluster1=49 and Cluster2=49, Figure 2E–2H). Subsequently, we performed immune infiltration analysis using two types of samples from the TCGA-ESCC and combined datasets (Figure 3I, 3J). In the two datasets, immune cells, such as central memory CD4 T cells, gamma delta T cells, MDSCs, and monocytes, had significant infiltration differences in different subtypes. This result indicated that MMRGs can characterize ESCC samples into two different subtypes based on mitochondrial metabolism.

Construction and prognostic analysis of MMRGs models

Based on the previous analysis, we quantified the impact of MMRGs on the prognosis of each ESCC patient and

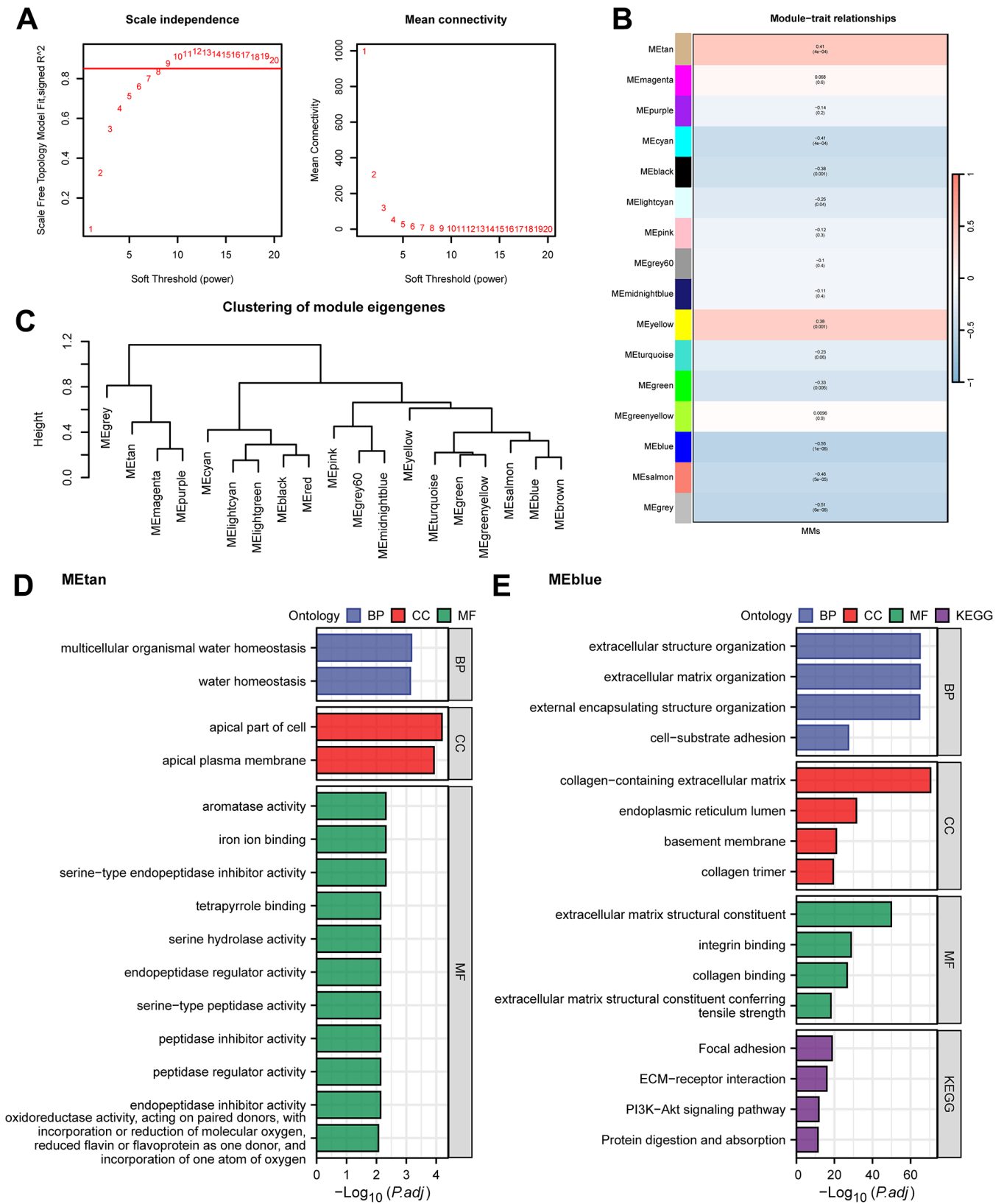


Figure 1. WGCNA analysis and GO/KEGG analysis. (A) WGCNA threshold screening graph. (B) The correlation heatmap between WGCNA module genes and MMs. (C) WGCNA module clustering tree. (D, E) GO/KEGG enrichment analysis of METan (D) module genes and MEblue (E) module genes.

constructed a risk model by integrating the expression of 152 MMRGs. Initially, 20 prognosis-related MMRGs were identified using univariate Cox regression with TCGA-ESCC (Figure 3A). Subsequently, LASSO regression was used to eliminate the collinearity of these 20 genes, determine the best lambda value and construct

cross validation (Figure 3B, 3C). Finally, we identified 6 prognostically relevant key genes (COX10, ACADVL, IDH3B, AKR1A1, LIAS, and NDUFB8), and based on these 6 genes we mapped the nomogram of prognostic risk (Figure 3D). According to the median value of the risk score, ESCC patients were divided into high- and

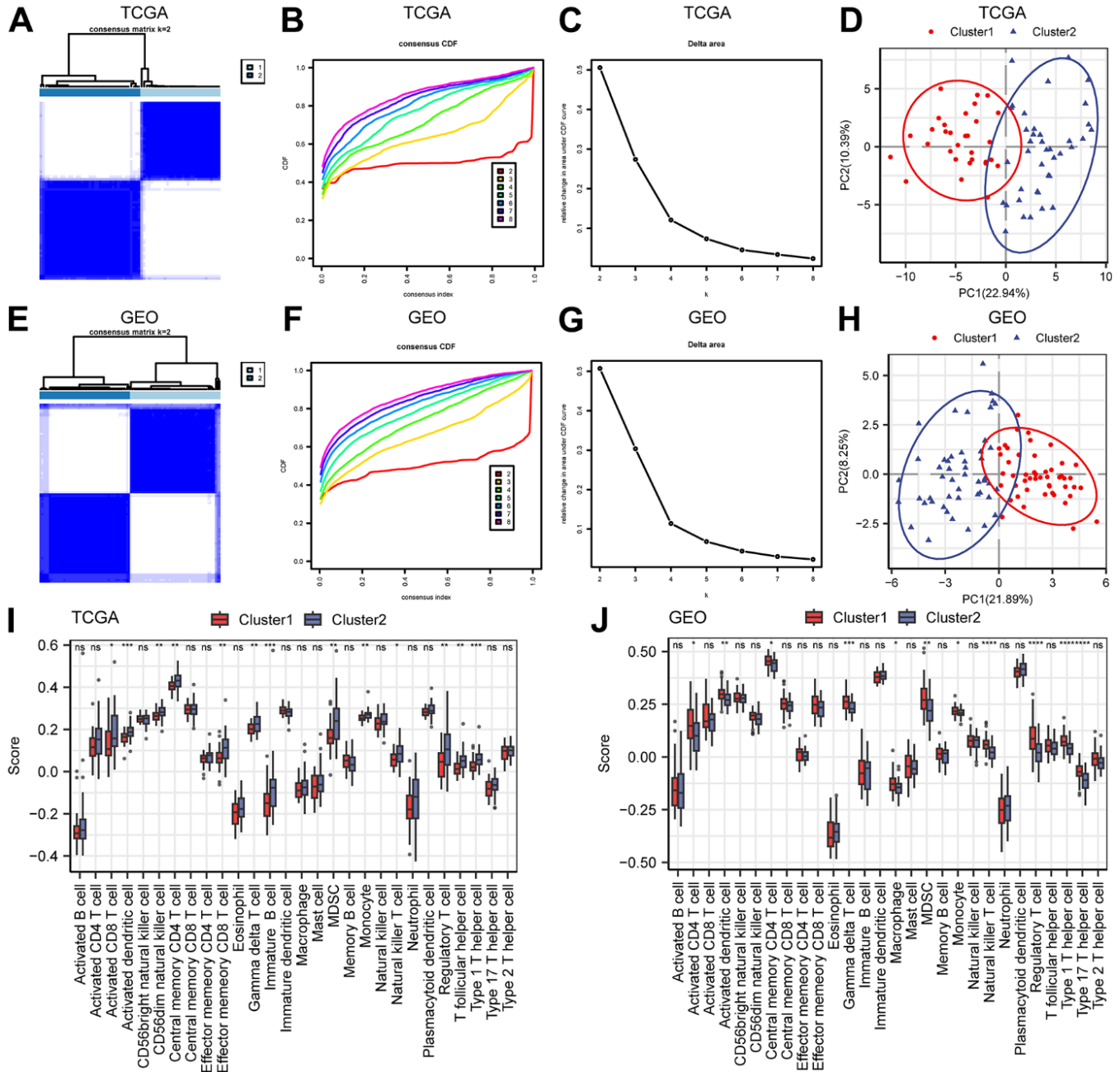


Figure 2. Construction of molecular subtypes. (A–C) The consistency clustering heatmap (A), consistency clustering cumulative distribution map (B), and consistency clustering Delta (C) of ESCC samples in the TCGA-ESCC dataset. (D) PCA diagram of TCGA-ESCC molecular subtypes. (E–G) Consistency clustering heatmap (E), consistency clustering cumulative distribution map (F), and consistency clustering Delta (G) of the merged GEO dataset. (H) PCA diagram of molecular subtypes in the merged GEO dataset. (I, J) Comparison of immune infiltration groups for different clusters in the TCGA-ESCC dataset (I) and the merged GEO dataset (J). Ns stands for $P \geq 0.05$, * for $P < 0.05$, ** for $P < 0.01$, *** for $P < 0.001$, and **** for $P < 0.0001$.

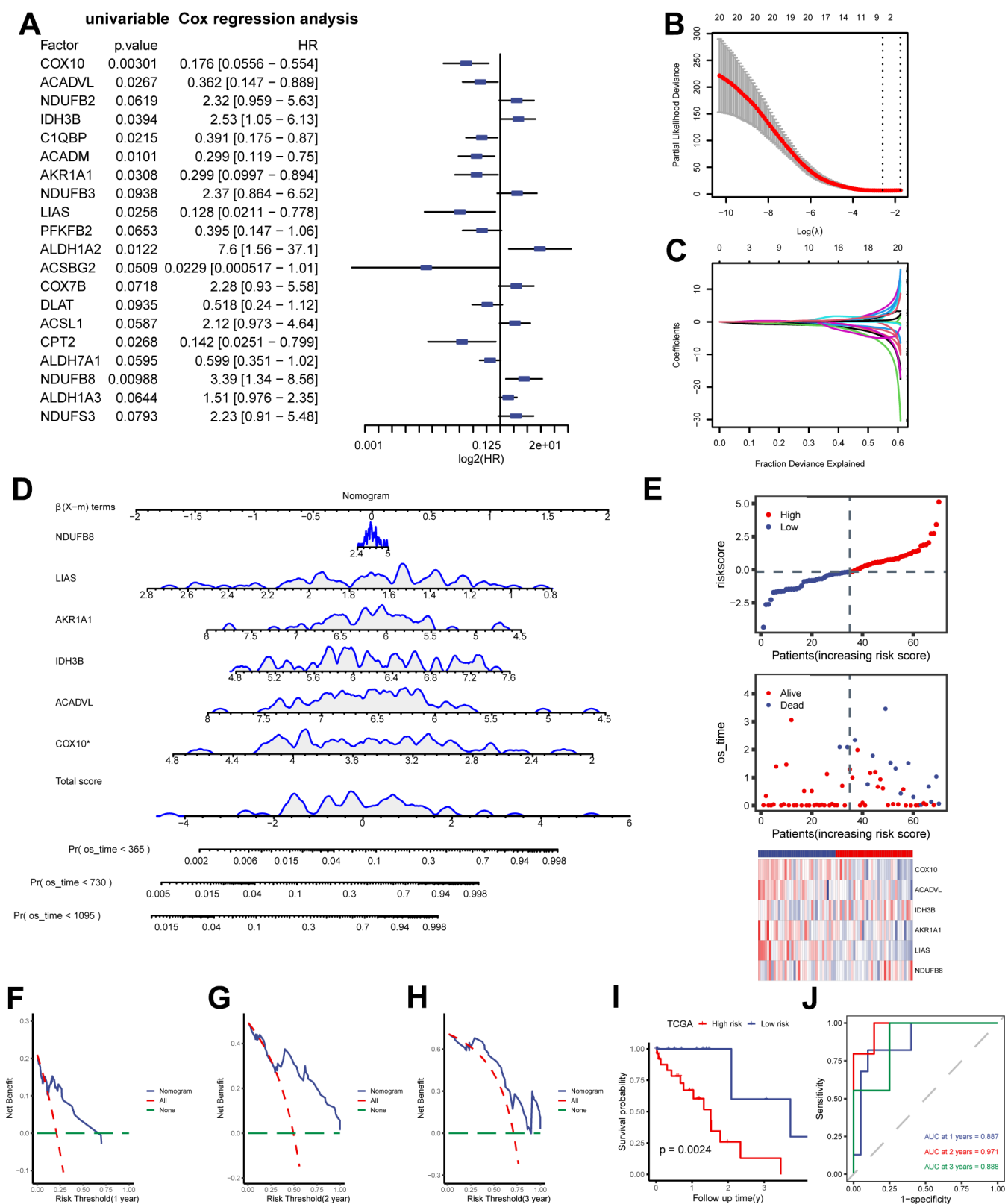


Figure 3. Construction of MMRGs prognostic model. (A) Cox univariable analysis forest map of MMRGs. (B, C) LASSO regression analysis variable trajectory diagram (B), variable screening diagram (C). (D, E) MMRGs Cox Multifactor Analysis nomogram (D), Risk group map (E). (F–H) Prognosis DCA map of Cox multivariate model at 1, 2, 3 years. (I, J) The KM curve (I) and ROC (J). MMRGs: Mitochondrial metabolism-related genes. LASSO: Least absolute shrinkage and selection operator. DCA: Decision curve analysis.

low-risk groups (Figure 3E). The DCA curves demonstrated the good predictive ability of the Cox model for 1-, 2-, and 3-year survival risk in ESCC patients (Figure 3F–3H). As expected, the K-M curve showed that patients in the high-risk score group had a worse prognosis than those in the low-risk score group (Figure 3I), and ROC also indicated a good predictive ability, with the highest predictive performance at 2 years (AUC=0.971, Figure 3J).

Comparative analysis between high and low risk groups

To identify DEGs between the two groups of patients, we conducted differential analysis, and a total of 399 genes ($P_{\text{adjust}} < 0.05$ and $|\log_{2}FC| > 1$) were identified (Supplementary Table 6 and Figure 4A). Furthermore, functional similarity analysis was performed, and the top 10 DEGs were MAB21L2, SNTG1, UPK1A, ANKRD45, AR, DIRAS2, ZIM3, ACTL8, TNFSF11, and TCF24 (Figure 4B). The results of the GO enrichment analysis demonstrated that BPs, such as axoneme assembly and meiotic cell cycle, and CCs, such as integral component of synaptic membrane and collagen trimer, were significantly enriched (Figure 4C). Additionally, the neuroactive ligand–receptor interaction pathway in KEGG was enriched (Supplementary Table 7 and Figure 4C, 4D). We also generated a correlation heatmap of the top 10 functionally similar genes, which showed that most of these genes exhibited significant positive correlations (Figure 4E). To further determine the influence of DEG expression between the two risk groups, we analysed the correlation between DEG and enriched pathways through GSEA (Supplementary Figure 4A and Supplementary Table 8). The results revealed that DEGs were significantly enriched in the IL 18 signalling pathway (Supplementary Figure 4B), oxidative phosphorylation (Supplementary Figure 4C), metabolism of polyamines (Supplementary Figure 4D), electron transport chain OXPHOS system in mitochondria (Supplementary Figure 4E), and electron transport (Supplementary Figure 4F and Supplementary Table 8).

Analysis of the interactions among key genes

To understand the wide range of associations among biomolecules, we used the GeneMANIA website to further analyse genes functionally associated with the 6 prognostically relevant key genes and constructed the interaction networks among them (Figure 5A). In addition, there is also a complex regulatory relationship between miRNAs and gene expression, so we predicted the mRNA–miRNA interaction network of these 6 genes with the help of miRDB database (Figure 5B). The network consisted of 5 key genes (COX10, ACADVL,

IDH3B, LIAS, and NDUFB8), 37 miRNA molecules, and 38 pairs of mRNA–miRNA interactions in total (Supplementary Table 9). Further, we analyzed the expression of these six genes in two risk subgroups (Figure 5C, 5D). Results revealed that COX10, ACADVL, AKR1A1, and LIAS exhibited significant expression differences and consistent expression trends in both TCGA-ESCC and combined-GEO datasets ($P < 0.05$).

Immune infiltration analysis

To understand the differences in immune cell infiltration in the tumour microenvironment between the two groups in the Cox model, infiltration was calculated using CIBERSORT with the TCGA-ESCC dataset (Supplementary Figure 5A, 5D). The correlation heatmap revealed that most immune cells were significantly correlated with activated mast cells and M0 macrophages (Supplementary Figure 5B). Additionally, correlation analysis of key genes also demonstrated that AKR1A1 is associated with the largest number of immune cells out of all the key genes (Supplementary Figure 5C).

SNP and CNV analysis

To compare mutations in the high- and low-risk groups in the TCGA-ESCC dataset, we generated a mutation waterfall plot, which demonstrated that TP53 exhibited the highest mutation frequency (Supplementary Figure 6A). Additionally, we conducted GISTIC 2.0 analysis on the CNV segments of the two groups (Supplementary Figure 6B–6E). The CNV analysis results revealed that the largest increase in the number of mutated CNVs was observed at 11q13.3, while the largest decrease in the number of CNVs occurred at 9q21.3 in both groups.

Construction of the clinical prognosis model based on the risk score

To improve the clinical predictability of the model, we constructed a predictive nomogram by combining the Cox risk score model with clinical characteristics. Firstly, we compared the differences in various clinical factors between the two groups of the Cox model (Supplementary Figure 7A–7F). Then univariate Cox analysis indicated that the risk score, sex, and N stage had P -values less than 0.1 and were included in the final model (Figure 6A). Finally, a nomogram was constructed, which could be utilized to determine the probability of survival for less than 1, 2 or 3 years (Figure 6B). To further evaluate the performance of the nomogram in comparison to that of other single factors, we plotted ROC curves within 3 years (Figure 6C–6E). The results suggested that the AUC values exceeded those of the other single factors and indicated that the

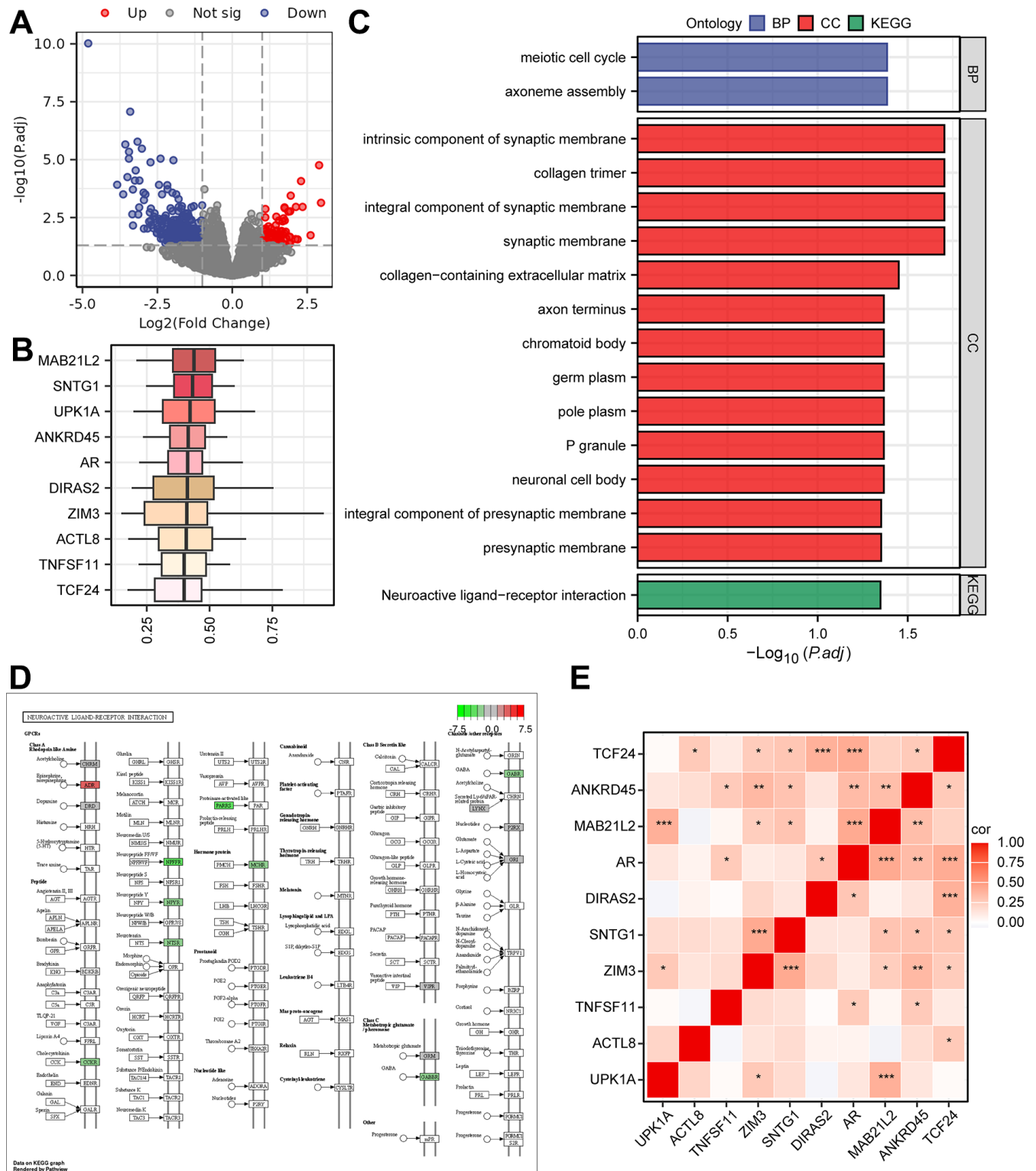


Figure 4. The results of Gene Ontology (GO) and KEGG pathway analyses. (A) Volcano plot of DEGs grouped as high- and low-risk using the Cox regression model. **(B)** Box plots showing the functional similarity analysis of the top 10 genes. **(C)** Bar plots displaying the results of GO and KEGG pathway enrichment analyses of the DEGs. **(D)** Pathway map for the Neuroactive ligand-receptor interaction pathway, with color mapping from green to red indicating increasing logFC values. **(E)** Correlation heatmap for the top 10 functionally similar genes.

molecular marker for predicting ESCC patient prognosis [39]. Considering that the development of ESCC is a complex clinical pathological process with genetic heterogeneity, a predictive model that integrates multiple factors may better assess the outcome of patients than a single biomarker.

Mitochondria are central to cell energy metabolism [5], and dysregulation of cellular energy metabolism is a significant characteristic of tumours [40]. Mitochondrial metabolism is involved in the malignant transformation of cells, tumour progression, therapeutic response and immune monitoring [41]. In ESCC, recent research has shown that circPUM1 localized in mitochondria and regulated the oxidative phosphorylation in cancer cell mitochondria to enhance the tumorigenicity of ESCC

cells *in vivo* and *in vitro* [42]. Similarly, researchers have found that STAT3 β can disrupt the electron transport chain of mitochondria and enhance the chemosensitivity of ESCC cells [43]. Therefore, in this study, we demonstrated the heterogeneity of mitochondrial metabolism in ESCC patients and identified a gene signature of MMRGs related to ESCC. Finally, we constructed a more reliable clinical prediction model by combining the clinical characteristics of patients and the 6-gene prognostic signature.

In our study, we identified co-expression modules of ESCC genes through WGCNA and found a significant correlation between ESCC modules and MMs. Among them, the genes in the modules with the strongest positive and negative correlation ($r=0.41$ and $r=-0.55$) were

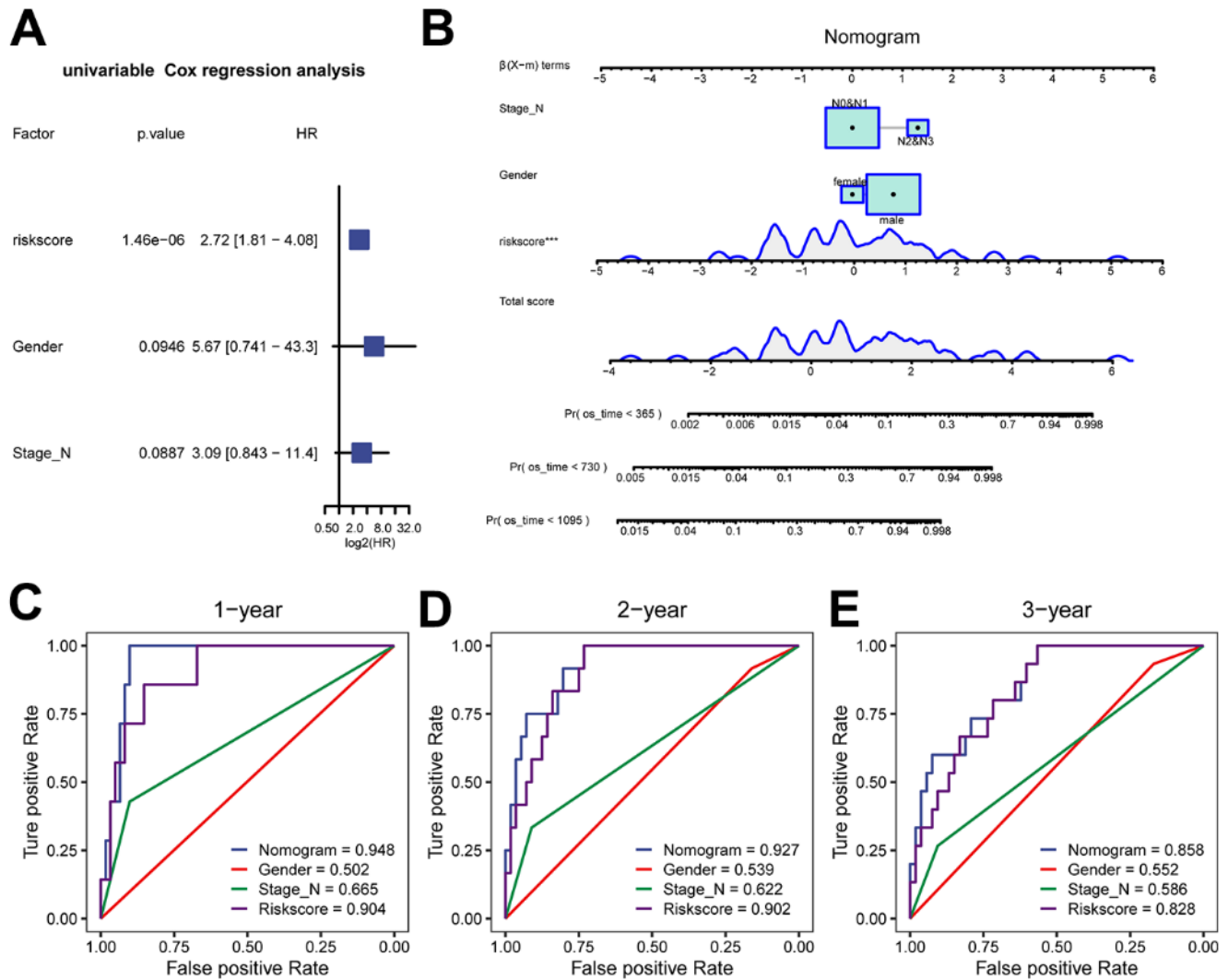


Figure 6. Clinical prediction model based on risk score in the TCGA-ESCC dataset. (A) Forest plot of univariate analysis for the clinical prediction model. (B) Nomogram of the clinical prediction model for multivariate analysis. (C-E) ROC curves of the clinical prediction model for 1 year (C), 2 years (D), and 3 years (E) compared to single factors.

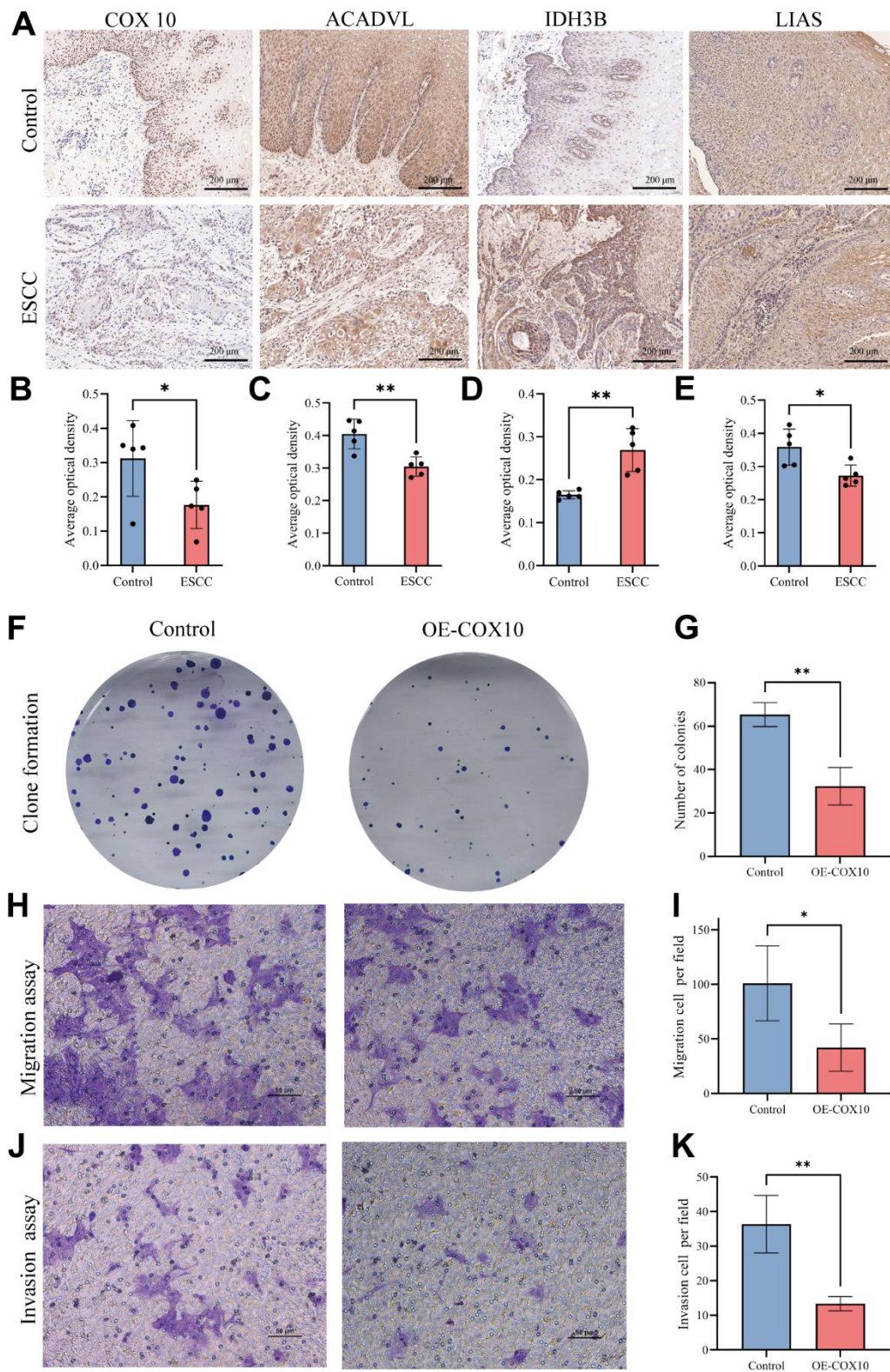


Figure 7. The expression of MMRGs and the role of COX10 protein in ESCC. (A) Representative image of the IHC staining of COX10, ACADVL, IDH3B and LIAS. (B–E) Quantitative statistics of the expression of COX10 (B), ACADVL (C), IDH3B (D) and LIAS (E). (F) Colony formation of ESCC cells transfected with COX10 or vector. (G) Quantitative statistics of the Colonies. (H) The migration ability of ESCC cells transfected with COX10 or vector. (I) Quantitative statistics of the migration cells per field. (J) The invasion ability in ESCC cells transfected with COX10 or vector. (K) Quantitative statistics of the invasion cells per field. Each experiment was repeated three times independently, and * stands for $P < 0.05$, ** stands for $P < 0.01$.

significantly enriched in mitochondrial metabolism, and specifically oxidoreductase activity acting on paired donors with incorporation or reduction of molecular oxygen. Furthermore, based on MMRGs, all patients can be divided into two subtypes through unsupervised clustering, which further confirms the important role of mitochondrial metabolism in ESCC, as was reported in previous studies. Notably, the pattern of immune infiltration varied between the two subtypes of patients; this variation is consistent with the results showing that mitochondrial metabolism is involved in cancer cell immune monitoring. For example, the infiltration of MSDC in immunosuppressive cells showed significant differences in the two subtypes ($p < 0.001$ in TCGA and $p < 0.05$ in GEO), and mitochondrial oxidative phosphorylation could promote the differentiation of MSDC and drive its immunosuppressive function [41, 44]. The infiltration scores of some immune cells in ESCC differed somewhat between the TCGA-ESCC and combined-GEO dataset due to the technical platform differences and biological variability between the sample sources, but this did not affect our conclusion that the immune microenvironment of ESCC with different mitochondrial metabolic states differed. More specific studies are still needed in the future to explore the complex crosstalk between mitochondrial metabolism and tumour immunity. In summary, MMRGs have remarkable potential in the prediction of ESCC patient prognosis.

The use of gene signatures to construct predictive models is a novel research method for identifying tumour prognostic biomarkers. Song et al. developed an immune signature to evaluate the outcomes of lung cancer patients [45], and Tong et al. similarly developed mitochondrial metabolism-related gene signatures for acute myeloid leukaemia [46]. For ESCC, a 5-gene prognostic signature based on m6A RNA methylation and a 10-genes related to ferroptosis was constructed, and the prediction performance was good, with the best accuracy of approximately 75% [47, 48]. However, the prediction of patient prognosis based on these gene signatures often lacks clinical correlation. In the present study, we found differences in multiple clinical features of ESCC patients in the high and low MMs groups, such as age, sex and N stage. After constructing a model based on our MMs signature, we conducted univariate Cox analysis to identify the clinical characteristics related to prognosis risk (sex and N stage) and included them in our model. Finally, a clinical prediction model was constructed. Remarkably, the MMRG signature combined with clinical features could predict the outcomes of ESCC patients in 3 years with AUCs of 0.948, 0.927, and 0.858, which are generally higher than those of previous models (0.600 in the m6A RNA signature [47] and 0.751 in the ferroptosis-related

signature [48]). Altogether, we built a novel clinical prediction model for ESCC based on the MMRG signature, and the predictive value was generally higher than that of previous predictive models.

To identify the MMRGs gene signature for prognostic models, we systematically investigated the 152 MMRGs in patients with ESCC. Finally, 6 core genes (COX10, ACADVL, IDH3B, AKR1A1, LIAS, and NDUFB8) were identified through the LASSO regression algorithm and included in our MMRGs signature for multivariable Cox regression. Notably, most of these key genes are reportedly involved in various cancers. ACADVL variants result in long-chain acyl-CoA dehydrogenase deficiency in mitochondria [49], while recent research indicates that tumour-specific T cells can be metabolically reprogrammed via the forced expression of ACADVL, which promoted the survival of tumour-specific T cells in a pancreatic cancer mouse model and improve their immunotherapeutic effects [50]. ACADVL over-expression is important to leukaemia mitochondrial metabolism because the loss of ACADVL activity results in the repression of cell proliferation, clonogenic potential, and engraftment in leukaemia cells [51]. However, in our study, higher expression of ACADVL was associated with better outcomes in ESCC. The opposite effects of ACADVL might be driven by the different tumour microenvironments in solid tumours and haematologic tumours. IDH3 β is considered a novel APC/C-CDH1 substrate and an important regulator of the cell cycle that can promote cell proliferation in ESCC, and the overexpression of IDH3 β is often correlated with poor prognosis in ESCC [52]; this correlation is consistent with the high HR of IDH3 β in our study (HR=2.29). AKR1A1 is a member of the human aldo-keto reductase (AKR) family, which is widely distributed in most cancer cells with relatively stable abundances [53]. AKR1A1 expression increases following radiation of laryngeal cancer, thereby inhibiting the activation of p53; thus, AKR1A1 plays a role in acquired radiation resistance in laryngeal cancer cells [54]. Variant LIAS could result in defective mitochondrial metabolism [55]. High LIAS expression has been correlated with a better prognosis in multiple cancer patients, such as kidney carcinoma, rectum adenocarcinoma and breast cancer [56], and this correlation is consistent with our findings. NDUFB8 is a subunit of mitochondrial complex I, and the inhibition of NDUFB8 can mediate excessive ROS production and ATP depletion, which may induce apoptosis in gastric adenocarcinoma cells [57]. Notably, both our univariate and multivariate regression analyses indicated that COX10 is a key gene in mitochondrial metabolism in ESCC. COX10 promotes the assembly of mitochondrial electron transport complex IV, an essential component of the mitochondrial respiratory chain [58]. In lung

cancer and melanoma, although COX10 deficiency reduces tumour neovascularization and slows tumour growth, it likewise leads to an increase in the area of avascular necrosis and promote tumour metastasis [59]. In addition, COX10-deficient cells upregulate glycolysis, which is the backbone of tumour cell metabolism [60, 61]. Thus, COX10 deficiency does more harm than good during tumour progression. In our study COX10 was significantly lower-expressed in the ESCC high-risk group in our study and was involved in the outcome of ESCC, which is consistent with this view. In addition, our *in vitro* experiments did find that in overexpression of COX10 could significantly inhibit the proliferation, migration and invasion ability of ESCC cells. Interestingly, previous reports have shown that multiple miRNAs can regulate the COX10 expression [58, 62]. In our interaction network analysis, COX10 similarly interacts with multiple miRNAs, suggesting that the expression of key genes for mitochondrial metabolism is multiply regulated in ESCC and cannot be simply generalized. Meanwhile, the crosstalk between these molecules also provides important clues for subsequent studies. In summary, our analysis indicated that key genes in the MMRG signature play an important role in the prognosis of ESCC patients, although previous studies have rarely reported their role in ESCC.

Certainly, there are some limitations to our study. First, the combined dataset did not contain prognostic information; thus, external validation of the clinical prediction model was not possible. Second, this study utilized public datasets for analysis, so there may be some inevitable selection biases. Otherwise, how these MMRGs affect the pathways and mechanisms of ESCC biogenesis needs to be explored through in-depth experiments. Finally, as limited by the original data, this study did not fully consider the impact of the location of oesophageal cancer and treatment methods, but the prediction rate of this study was above 90%; thus, this model is still very valuable.

CONCLUSIONS

In conclusion, we investigated dysregulated mitochondrial metabolism-associated pathways in ESCC, and a novel 6 MMRGs signature in ESCC patients was developed that could accurately predict prognosis outcomes. This study might provide novel insights into predicting clinical outcomes of ESCC patients.

Abbreviations

MMRGs: Mitochondrial metabolism-related genes; MMs: Mitochondrial metabolism scores; SNP: Single nucleotide polymorphism; CNV: Copy Number

Variation; MMs: Mitochondrial energy metabolism score; WGCNA: Weighted gene co-expression network analysis; GO: Gene Ontology; BP: Biological process; CC: Cellular component; MF: Molecular function; KEGG: Kyoto Encyclopedia of Genes and Genomes.

AUTHOR CONTRIBUTIONS

Conception and design of the work: ZX, WL and CY. Acquisition, analysis, visualization and interpretation of data: LS, ZC, CQ, MZ, JL and RK. Performing the experiments: LS and WL. Writing – original draft: WL and CY. Writing – review and editing, study supervision: ZX. All authors have read and approved the final draft for publication. All authors contributed to the article and approved the submitted version.

CONFLICTS OF INTEREST

The authors declare that they have no conflicts of interest.

ETHICAL STATEMENT AND CONSENT

Patients were informed that the resected specimens were stored by the hospital and potentially used for scientific research, and that their privacy would be maintained. All patients provided informed consent prior to undergoing surgery. Our study protocol (approval number: 2021113) was approved by The Ethics Committee of The Second Affiliated Hospital of Xi'an Jiaotong University.

FUNDING

This work was funded by grants from the National Natural Science Foundation of China (Grant serial number: 82303811), the Natural Science Basic Research Program of Shaanxi Province (Grant serial number: 2023-JC-QN-0840) and the Key Research and Development Program of Shannxi Province (Grant serial numbers: S2023-YF-YBSF-0261).

REFERENCES

1. Sung H, Ferlay J, Siegel RL, Laversanne M, Soerjomataram I, Jemal A, Bray F. Global Cancer Statistics 2020: GLOBOCAN Estimates of Incidence and Mortality Worldwide for 36 Cancers in 185 Countries. *CA Cancer J Clin.* 2021; 71:209–49. <https://doi.org/10.3322/caac.21660> PMID:33538338
2. Morgan E, Soerjomataram I, Rungay H, Coleman HG, Thrift AP, Vignat J, Laversanne M, Ferlay J, Arnold M. The Global Landscape of Esophageal Squamous Cell Carcinoma and Esophageal Adenocarcinoma Incidence

- and Mortality in 2020 and Projections to 2040: New Estimates From GLOBOCAN 2020. *Gastroenterology*. 2022; 163:649–58.e2.
<https://doi.org/10.1053/j.gastro.2022.05.054>
PMID:35671803
3. He S, Xu J, Liu X, Zhen Y. Advances and challenges in the treatment of esophageal cancer. *Acta Pharm Sin B*. 2021; 11:3379–92.
<https://doi.org/10.1016/j.apsb.2021.03.008>
PMID:34900524
 4. Thrift AP. Global burden and epidemiology of Barrett oesophagus and oesophageal cancer. *Nat Rev Gastroenterol Hepatol*. 2021; 18:432–43.
<https://doi.org/10.1038/s41575-021-00419-3>
PMID:33603224
 5. Ji W, Tang X, Du W, Lu Y, Wang N, Wu Q, Wei W, Liu J, Yu H, Ma B, Li L, Huang W. Optical/electrochemical methods for detecting mitochondrial energy metabolism. *Chem Soc Rev*. 2022; 51:71–127.
<https://doi.org/10.1039/d0cs01610a>
PMID:34792041
 6. Zong WX, Rabinowitz JD, White E. Mitochondria and Cancer. *Mol Cell*. 2016; 61:667–76.
<https://doi.org/10.1016/j.molcel.2016.02.011>
PMID:26942671
 7. Li SH, Nofal M, Parsons LR, Rabinowitz JD, Gitai Z. Monitoring mammalian mitochondrial translation with MitoRiboSeq. *Nat Protoc*. 2021; 16:2802–25.
<https://doi.org/10.1038/s41596-021-00517-1>
PMID:33953394
 8. Egan G, Khan DH, Lee JB, Mirali S, Zhang L, Schimmer AD. Mitochondrial and Metabolic Pathways Regulate Nuclear Gene Expression to Control Differentiation, Stem Cell Function, and Immune Response in Leukemia. *Cancer Discov*. 2021; 11:1052–66.
<https://doi.org/10.1158/2159-8290.CD-20-1227>
PMID:33504581
 9. Liu Z, Gu S, Lu T, Wu K, Li L, Dong C, Zhou Y. IF16 depletion inhibits esophageal squamous cell carcinoma progression through reactive oxygen species accumulation via mitochondrial dysfunction and endoplasmic reticulum stress. *J Exp Clin Cancer Res*. 2020; 39:144.
<https://doi.org/10.1186/s13046-020-01646-3>
PMID:32727517
 10. Gao X, Xu M, Wang H, Xia Z, Sun H, Liu M, Zhao S, Yang F, Niu Z, Gao H, Zhu H, Lu J, Zhou X. Development and validation of a mitochondrial energy metabolism-related risk model in hepatocellular carcinoma. *Gene*. 2023; 855:147133.
<https://doi.org/10.1016/j.gene.2022.147133>
PMID:36565797
 11. Ye Z, Zhang H, Kong F, Lan J, Yi S, Jia W, Zheng S, Guo Y, Zhan X. Comprehensive Analysis of Alteration Landscape and Its Clinical Significance of Mitochondrial Energy Metabolism Pathway-Related Genes in Lung Cancers. *Oxid Med Cell Longev*. 2021; 2021:9259297.
<https://doi.org/10.1155/2021/9259297>
PMID:34970420
 12. Cao Z, Lin J, Fu G, Niu L, Yang Z, Cai W. An integrated bioinformatic investigation of mitochondrial energy metabolism genes in colon adenocarcinoma followed by preliminary validation of CPT2 in tumor immune infiltration. *Front Immunol*. 2022; 13:959967.
<https://doi.org/10.3389/fimmu.2022.959967>
PMID:36177002
 13. Yang H, Cui Y, Zhu Y. Comprehensive analysis reveals signal and molecular mechanism of mitochondrial energy metabolism pathway in pancreatic cancer. *Front Genet*. 2023; 14:1117145.
<https://doi.org/10.3389/fgene.2023.1117145>
PMID:36814901
 14. Tong X, Zhou F. Integrated bioinformatic analysis of mitochondrial metabolism-related genes in acute myeloid leukemia. *Front Immunol*. 2023; 14:1120670.
<https://doi.org/10.3389/fimmu.2023.1120670>
PMID:37138869
 15. Colaprico A, Silva TC, Olsen C, Garofano L, Cava C, Garolini D, Sabedot TS, Malta TM, Pagnotta SM, Castiglioni I, Ceccarelli M, Bontempi G, Noushmehr H. TCGAbiolinks: an R/Bioconductor package for integrative analysis of TCGA data. *Nucleic Acids Res*. 2016; 44:e71.
<https://doi.org/10.1093/nar/gkv1507> PMID:26704973
 16. Mayakonda A, Lin DC, Assenov Y, Plass C, Koeffler HP. Maftools: efficient and comprehensive analysis of somatic variants in cancer. *Genome Res*. 2018; 28:1747–56.
<https://doi.org/10.1101/gr.239244.118>
PMID:30341162
 17. Gao J, Aksoy BA, Dogrusoz U, Dresdner G, Gross B, Sumer SO, Sun Y, Jacobsen A, Sinha R, Larsson E, Cerami E, Sander C, Schultz N. Integrative analysis of complex cancer genomics and clinical profiles using the cBioPortal. *Sci Signal*. 2013; 6:p11.
<https://doi.org/10.1126/scisignal.2004088>
PMID:23550210
 18. Hu N, Clifford RJ, Yang HH, Wang C, Goldstein AM, Ding T, Taylor PR, Lee MP. Genome wide analysis of DNA copy number neutral loss of heterozygosity (CNNLOH) and its relation to gene expression in esophageal squamous cell carcinoma. *BMC Genomics*. 2010; 11:576.
<https://doi.org/10.1186/1471-2164-11-576>
PMID:20955586

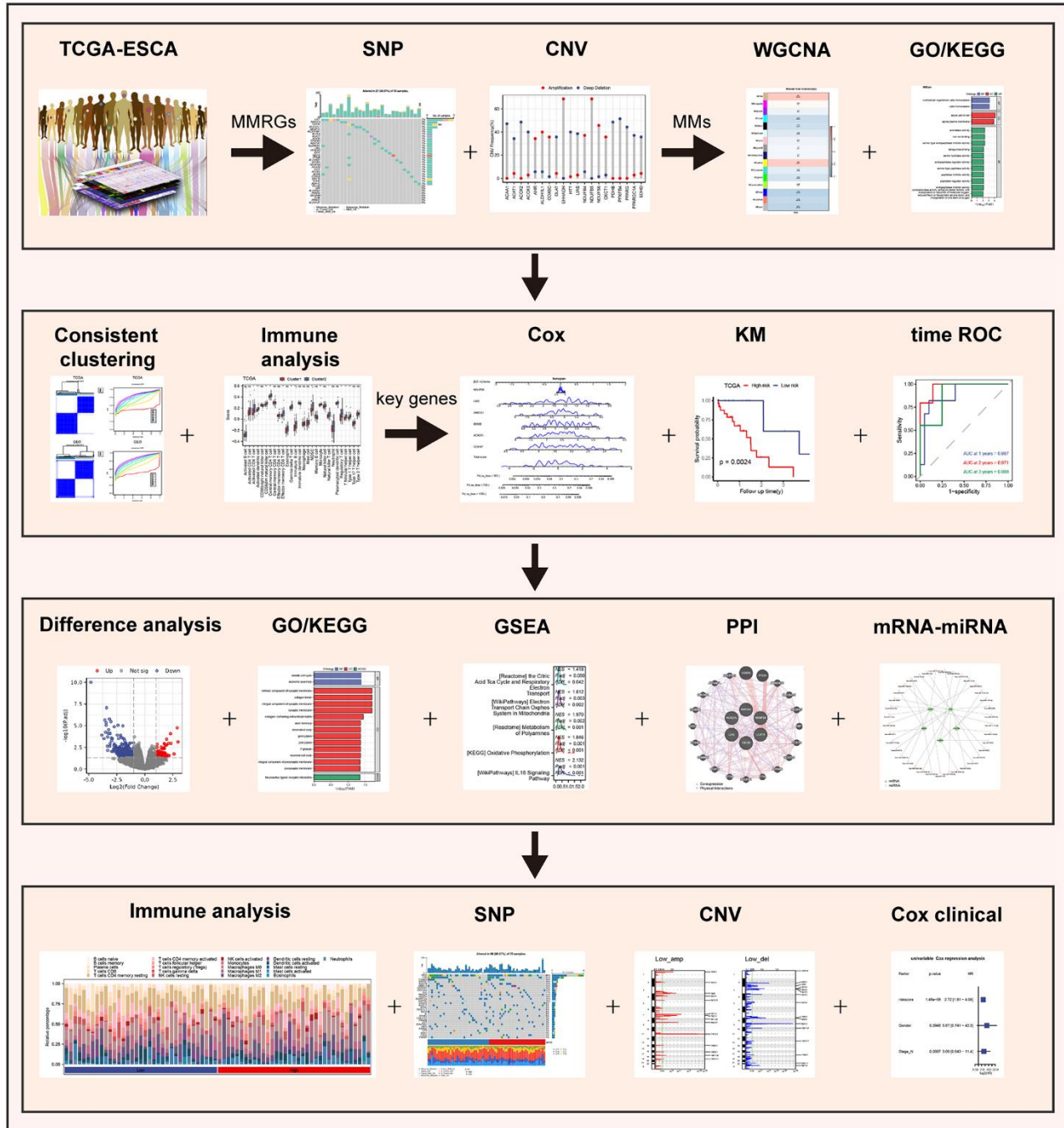
19. Su H, Hu N, Yang HH, Wang C, Takikita M, Wang QH, Giffen C, Clifford R, Hewitt SM, Shou JZ, Goldstein AM, Lee MP, Taylor PR. Global gene expression profiling and validation in esophageal squamous cell carcinoma and its association with clinical phenotypes. *Clin Cancer Res*. 2011; 17:2955–66.
<https://doi.org/10.1158/1078-0432.CCR-10-2724>
PMID:[21385931](https://pubmed.ncbi.nlm.nih.gov/21385931/)
20. Davis S, Meltzer PS. GEOquery: a bridge between the Gene Expression Omnibus (GEO) and BioConductor. *Bioinformatics*. 2007; 23:1846–7.
<https://doi.org/10.1093/bioinformatics/btm254>
PMID:[17496320](https://pubmed.ncbi.nlm.nih.gov/17496320/)
21. Hänzelmann S, Castelo R, Guinney J. GSEA: gene set variation analysis for microarray and RNA-seq data. *BMC Bioinformatics*. 2013; 14:7.
<https://doi.org/10.1186/1471-2105-14-7>
PMID:[23323831](https://pubmed.ncbi.nlm.nih.gov/23323831/)
22. Langfelder P, Horvath S. WGCNA: an R package for weighted correlation network analysis. *BMC Bioinformatics*. 2008; 9:559.
<https://doi.org/10.1186/1471-2105-9-559>
PMID:[19114008](https://pubmed.ncbi.nlm.nih.gov/19114008/)
23. Yu G, Wang LG, Han Y, He QY. clusterProfiler: an R package for comparing biological themes among gene clusters. *OMICS*. 2012; 16:284–7.
<https://doi.org/10.1089/omi.2011.0118>
PMID:[22455463](https://pubmed.ncbi.nlm.nih.gov/22455463/)
24. Yu G. Gene Ontology Semantic Similarity Analysis Using GOSemSim. *Methods Mol Biol*. 2020; 2117:207–15.
https://doi.org/10.1007/978-1-0716-0301-7_11
PMID:[31960380](https://pubmed.ncbi.nlm.nih.gov/31960380/)
25. Kanehisa M, Goto S. KEGG: kyoto encyclopedia of genes and genomes. *Nucleic Acids Res*. 2000; 28:27–30.
<https://doi.org/10.1093/nar/28.1.27> PMID:[10592173](https://pubmed.ncbi.nlm.nih.gov/10592173/)
26. Wilkerson MD, Hayes DN. ConsensusClusterPlus: a class discovery tool with confidence assessments and item tracking. *Bioinformatics*. 2010; 26:1572–3.
<https://doi.org/10.1093/bioinformatics/btq170>
PMID:[20427518](https://pubmed.ncbi.nlm.nih.gov/20427518/)
27. Barbie DA, Tamayo P, Boehm JS, Kim SY, Moody SE, Dunn IF, Schinzel AC, Sandy P, Meylan E, Scholl C, Fröhling S, Chan EM, Sos ML, et al. Systematic RNA interference reveals that oncogenic KRAS-driven cancers require TBK1. *Nature*. 2009; 462:108–12.
<https://doi.org/10.1038/nature08460>
PMID:[19847166](https://pubmed.ncbi.nlm.nih.gov/19847166/)
28. Park SY. Nomogram: An analogue tool to deliver digital knowledge. *J Thorac Cardiovasc Surg*. 2018; 155:1793.
<https://doi.org/10.1016/j.jtcvs.2017.12.107>
PMID:[29370910](https://pubmed.ncbi.nlm.nih.gov/29370910/)
29. Tataranni T, Piccoli C. Dichloroacetate (DCA) and Cancer: An Overview towards Clinical Applications. *Oxid Med Cell Longev*. 2019; 2019:8201079.
<https://doi.org/10.1155/2019/8201079>
PMID:[31827705](https://pubmed.ncbi.nlm.nih.gov/31827705/)
30. Yu G, Li F, Qin Y, Bo X, Wu Y, Wang S. GOSemSim: an R package for measuring semantic similarity among GO terms and gene products. *Bioinformatics*. 2010; 26:976–8.
<https://doi.org/10.1093/bioinformatics/btq064>
PMID:[20179076](https://pubmed.ncbi.nlm.nih.gov/20179076/)
31. Subramanian A, Tamayo P, Mootha VK, Mukherjee S, Ebert BL, Gillette MA, Paulovich A, Pomeroy SL, Golub TR, Lander ES, Mesirov JP. Gene set enrichment analysis: a knowledge-based approach for interpreting genome-wide expression profiles. *Proc Natl Acad Sci USA*. 2005; 102:15545–50.
<https://doi.org/10.1073/pnas.0506580102>
PMID:[16199517](https://pubmed.ncbi.nlm.nih.gov/16199517/)
32. Liberzon A, Birger C, Thorvaldsdóttir H, Ghandi M, Mesirov JP, Tamayo P. The Molecular Signatures Database (MSigDB) hallmark gene set collection. *Cell Syst*. 2015; 1:417–25.
<https://doi.org/10.1016/j.cels.2015.12.004>
PMID:[26771021](https://pubmed.ncbi.nlm.nih.gov/26771021/)
33. Franz M, Rodriguez H, Lopes C, Zuberi K, Montojo J, Bader GD, Morris Q. GeneMANIA update 2018. *Nucleic Acids Res*. 2018; 46:W60–4.
<https://doi.org/10.1093/nar/gky311> PMID:[29912392](https://pubmed.ncbi.nlm.nih.gov/29912392/)
34. Chen Y, Wang X. miRDB: an online database for prediction of functional microRNA targets. *Nucleic Acids Res*. 2020; 48:D127–31.
<https://doi.org/10.1093/nar/gkz757>
PMID:[31504780](https://pubmed.ncbi.nlm.nih.gov/31504780/)
35. Newman AM, Steen CB, Liu CL, Gentles AJ, Chaudhuri AA, Scherer F, Khodadoust MS, Esfahani MS, Luca BA, Steiner D, Diehn M, Alizadeh AA. Determining cell type abundance and expression from bulk tissues with digital cytometry. *Nat Biotechnol*. 2019; 37:773–82.
<https://doi.org/10.1038/s41587-019-0114-2>
PMID:[31061481](https://pubmed.ncbi.nlm.nih.gov/31061481/)
36. Mermel CH, Schumacher SE, Hill B, Meyerson ML, Beroukhim R, Getz G. GISTIC2.0 facilitates sensitive and confident localization of the targets of focal somatic copy-number alteration in human cancers. *Genome Biol*. 2011; 12:R41.
<https://doi.org/10.1186/gb-2011-12-4-r41>
PMID:[21527027](https://pubmed.ncbi.nlm.nih.gov/21527027/)
37. Xu Z, Zheng J, Chen Z, Guo J, Li X, Wang X, Qu C, Yuan L, Cheng C, Sun X, Yu J. Multilevel regulation of Wnt signaling by Zic2 in colon cancer due to mutation of β -catenin. *Cell Death Dis*. 2021; 12:584.

- <https://doi.org/10.1038/s41419-021-03863-w>
PMID:[34099631](https://pubmed.ncbi.nlm.nih.gov/34099631/)
38. Wu Q, Zhang W, Wang Y, Min Q, Zhang H, Dong D, Zhan Q. MAGE-C3 promotes cancer metastasis by inducing epithelial-mesenchymal transition and immunosuppression in esophageal squamous cell carcinoma. *Cancer Commun (Lond)*. 2021; 41:1354–72. <https://doi.org/10.1002/cac2.12203> PMID:[34347390](https://pubmed.ncbi.nlm.nih.gov/34347390/)
39. Cui Y, Chen H, Xi R, Cui H, Zhao Y, Xu E, Yan T, Lu X, Huang F, Kong P, Li Y, Zhu X, Wang J, et al. Whole-genome sequencing of 508 patients identifies key molecular features associated with poor prognosis in esophageal squamous cell carcinoma. *Cell Res*. 2020; 30:902–13. <https://doi.org/10.1038/s41422-020-0333-6> PMID:[32398863](https://pubmed.ncbi.nlm.nih.gov/32398863/)
40. Hanahan D. Hallmarks of Cancer: New Dimensions. *Cancer Discov*. 2022; 12:31–46. <https://doi.org/10.1158/2159-8290.CD-21-1059> PMID:[35022204](https://pubmed.ncbi.nlm.nih.gov/35022204/)
41. Porporato PE, Filigheddu N, Pedro JM, Kroemer G, Galluzzi L. Mitochondrial metabolism and cancer. *Cell Res*. 2018; 28:265–80. <https://doi.org/10.1038/cr.2017.155> PMID:[29219147](https://pubmed.ncbi.nlm.nih.gov/29219147/)
42. Gong W, Xu J, Wang Y, Min Q, Chen X, Zhang W, Chen J, Zhan Q. Nuclear genome-derived circular RNA circPUM1 localizes in mitochondria and regulates oxidative phosphorylation in esophageal squamous cell carcinoma. *Signal Transduct Target Ther*. 2022; 7:40. <https://doi.org/10.1038/s41392-021-00865-0> PMID:[35153295](https://pubmed.ncbi.nlm.nih.gov/35153295/)
43. Zheng ZY, Yang PL, Li RY, Liu LX, Xu XE, Liao LD, Li X, Chu MY, Peng L, Huang QF, Heng JH, Wang SH, Wu ZY, et al. STAT3 β disrupted mitochondrial electron transport chain enhances chemosensitivity by inducing pyroptosis in esophageal squamous cell carcinoma. *Cancer Lett*. 2021; 522:171–83. <https://doi.org/10.1016/j.canlet.2021.09.035> PMID:[34571081](https://pubmed.ncbi.nlm.nih.gov/34571081/)
44. Mohammadpour H, MacDonald CR, McCarthy PL, Abrams SI, Repasky EA. β 2-adrenergic receptor signaling regulates metabolic pathways critical to myeloid-derived suppressor cell function within the TME. *Cell Rep*. 2021; 37:109883. <https://doi.org/10.1016/j.celrep.2021.109883> PMID:[34706232](https://pubmed.ncbi.nlm.nih.gov/34706232/)
45. Song Q, Shang J, Yang Z, Zhang L, Zhang C, Chen J, Wu X. Identification of an immune signature predicting prognosis risk of patients in lung adenocarcinoma. *J Transl Med*. 2019; 17:70. <https://doi.org/10.1186/s12967-019-1824-4> PMID:[30832680](https://pubmed.ncbi.nlm.nih.gov/30832680/)
46. Liu Y, Wu L, Ao H, Zhao M, Leng X, Liu M, Ma J, Zhu J. Prognostic implications of autophagy-associated gene signatures in non-small cell lung cancer. *Aging (Albany NY)*. 2019; 11:11440–62. <https://doi.org/10.18632/aging.102544> PMID:[31811814](https://pubmed.ncbi.nlm.nih.gov/31811814/)
47. Guo W, Tan F, Huai Q, Wang Z, Shao F, Zhang G, Yang Z, Li R, Xue Q, Gao S, He J. Comprehensive Analysis of PD-L1 Expression, Immune Infiltrates, and m6A RNA Methylation Regulators in Esophageal Squamous Cell Carcinoma. *Front Immunol*. 2021; 12:669750. <https://doi.org/10.3389/fimmu.2021.669750> PMID:[34054840](https://pubmed.ncbi.nlm.nih.gov/34054840/)
48. Zhu J, Zhao Y, Wu G, Zhang X, Chen Q, Yang B, Guo X, Ji S, Gu K. Ferroptosis-Related lncRNA Signature Correlates with the Prognosis, Tumor Microenvironment, and Therapeutic Sensitivity of Esophageal Squamous Cell Carcinoma. *Oxid Med Cell Longev*. 2022; 2022:7465880. <https://doi.org/10.1155/2022/7465880> PMID:[35903713](https://pubmed.ncbi.nlm.nih.gov/35903713/)
49. Chen T, Tong F, Wu XY, Zhu L, Yi QZ, Zheng J, Yang RL, Zhao ZY, Cang XH, Shu Q, Jiang PP. Novel ACADVL variants resulting in mitochondrial defects in long-chain acyl-CoA dehydrogenase deficiency. *J Zhejiang Univ Sci B*. 2020; 21:885–96. <https://doi.org/10.1631/jzus.B2000339> PMID:[33150772](https://pubmed.ncbi.nlm.nih.gov/33150772/)
50. Manzo T, Prentice BM, Anderson KG, Raman A, Schalck A, Codreanu GS, Nava Lauson CB, Tiberti S, Raimondi A, Jones MA, Reyzer M, Bates BM, Spraggins JM, et al. Accumulation of long-chain fatty acids in the tumor microenvironment drives dysfunction in intrapancreatic CD8 $^{+}$ T cells. *J Exp Med*. 2020; 217:e20191920. <https://doi.org/10.1084/jem.20191920> PMID:[32491160](https://pubmed.ncbi.nlm.nih.gov/32491160/)
51. Tchong M, Roma A, Ahmed N, Smith RW, Jayanth P, Minden MD, Schimmer AD, Hess DA, Hope K, Rea KA, Akhtar TA, Bohrsen E, D'Alessandro A, et al. Very long chain fatty acid metabolism is required in acute myeloid leukemia. *Blood*. 2021; 137:3518–32. <https://doi.org/10.1182/blood.2020008551> PMID:[33720355](https://pubmed.ncbi.nlm.nih.gov/33720355/)
52. Wu Q, Zhang W, Xue L, Wang Y, Fu M, Ma L, Song Y, Zhan QM. APC/C-CDH1-Regulated IDH3 β Coordinates with the Cell Cycle to Promote Cell Proliferation. *Cancer Res*. 2019; 79:3281–93. <https://doi.org/10.1158/0008-5472.CAN-18-2341> PMID:[31053633](https://pubmed.ncbi.nlm.nih.gov/31053633/)
53. Zhang S, Wen B, Zhou B, Yang L, Cha C, Xu S, Qiu X, Wang Q, Sun H, Lou X, Zi J, Zhang Y, Lin L, Liu S. Quantitative analysis of the human AKR family

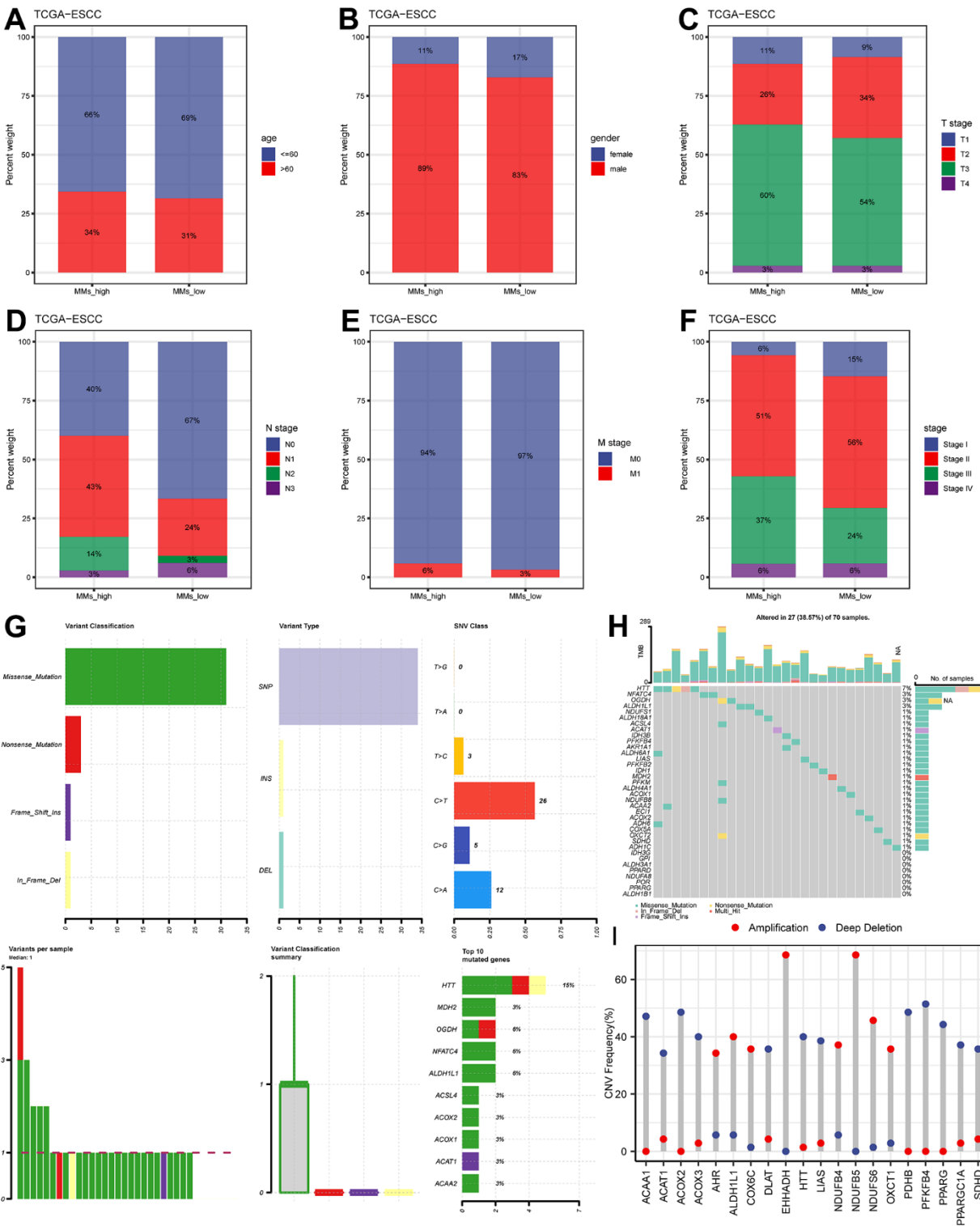
- members in cancer cell lines using the mTRAQ/MRM approach. *J Proteome Res.* 2013; 12:2022–33.
<https://doi.org/10.1021/pr301153z>
PMID:[23544749](https://pubmed.ncbi.nlm.nih.gov/23544749/)
54. Kim JS, Chang JW, Park JK, Hwang SG. Increased aldehyde reductase expression mediates acquired radioresistance of laryngeal cancer cells via modulating p53. *Cancer Biol Ther.* 2012; 13:638–46.
<https://doi.org/10.4161/cbt.20081>
PMID:[22555805](https://pubmed.ncbi.nlm.nih.gov/22555805/)
55. Mayr JA, Zimmermann FA, Fauth C, Bergheim C, Meierhofer D, Radmayr D, Zschocke J, Koch J, Sperl W. Lipoic acid synthetase deficiency causes neonatal-onset epilepsy, defective mitochondrial energy metabolism, and glycine elevation. *Am J Hum Genet.* 2011; 89:792–7.
<https://doi.org/10.1016/j.ajhg.2011.11.011>
PMID:[22152680](https://pubmed.ncbi.nlm.nih.gov/22152680/)
56. Cai Y, He Q, Liu W, Liang Q, Peng B, Li J, Zhang W, Kang F, Hong Q, Yan Y, Peng J, Xu Z, Bai N. Comprehensive analysis of the potential cuproptosis-related biomarker LIAS that regulates prognosis and immunotherapy of pan-cancers. *Front Oncol.* 2022; 12:952129.
<https://doi.org/10.3389/fonc.2022.952129>
PMID:[35982953](https://pubmed.ncbi.nlm.nih.gov/35982953/)
57. Wang H, Luo J, Tian W, Yan W, Ge S, Zhang Y, Sun W. γ -Tocotrienol inhibits oxidative phosphorylation and triggers apoptosis by inhibiting mitochondrial complex I subunit NDUF8 and complex II subunit SDHB. *Toxicology.* 2019; 417:42–53.
<https://doi.org/10.1016/j.tox.2019.01.018>
PMID:[30769052](https://pubmed.ncbi.nlm.nih.gov/30769052/)
58. Xu P, Palmer LE, Lechauve C, Zhao G, Yao Y, Luan J, Vourekas A, Tan H, Peng J, Schuetz JD, Mourelatos Z, Wu G, Weiss MJ, Paralkar VR. Regulation of gene expression by miR-144/451 during mouse erythropoiesis. *Blood.* 2019; 133:2518–28.
<https://doi.org/10.1182/blood.2018854604>
PMID:[30971389](https://pubmed.ncbi.nlm.nih.gov/30971389/)
59. Schiffmann LM, Werthenbach JP, Heintges-Kleinhofer F, Seeger JM, Fritsch M, Günther SD, Willenborg S, Brodesser S, Lucas C, Jüngst C, Albert MC, Schorn F, Witt A, et al. Mitochondrial respiration controls neoangiogenesis during wound healing and tumour growth. *Nat Commun.* 2020; 11:3653.
<https://doi.org/10.1038/s41467-020-17472-2>
PMID:[32694534](https://pubmed.ncbi.nlm.nih.gov/32694534/)
60. Mah-Som AY, Keppel MP, Tobin JM, Kolichski A, Saucier N, Sexl V, French AR, Wagner JA, Fehniger TA, Cooper MA. Reliance on Cox10 and oxidative metabolism for antigen-specific NK cell expansion. *Cell Rep.* 2021; 35:109209.
<https://doi.org/10.1016/j.celrep.2021.109209>
PMID:[34077722](https://pubmed.ncbi.nlm.nih.gov/34077722/)
61. Paul S, Ghosh S, Kumar S. Tumor glycolysis, an essential sweet tooth of tumor cells. *Semin Cancer Biol.* 2022; 86:1216–30.
<https://doi.org/10.1016/j.semcancer.2022.09.007>
PMID:[36330953](https://pubmed.ncbi.nlm.nih.gov/36330953/)
62. Chen Z, Li Y, Zhang H, Huang P, Luthra R. Hypoxia-regulated microRNA-210 modulates mitochondrial function and decreases ISCU and COX10 expression. *Oncogene.* 2010; 29:4362–8.
<https://doi.org/10.1038/onc.2010.193> PMID:[20498629](https://pubmed.ncbi.nlm.nih.gov/20498629/)

SUPPLEMENTARY MATERIALS

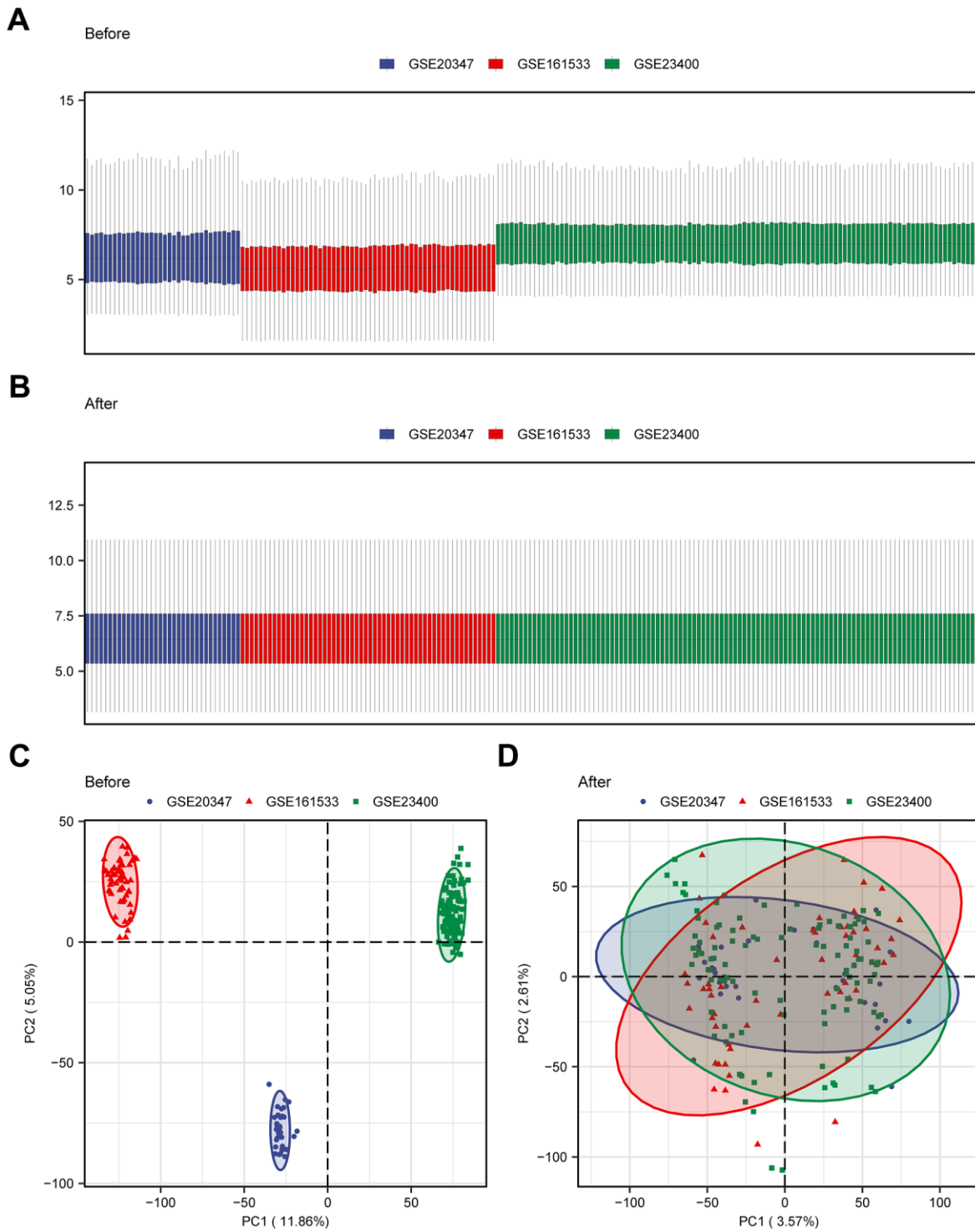
Supplementary Figures



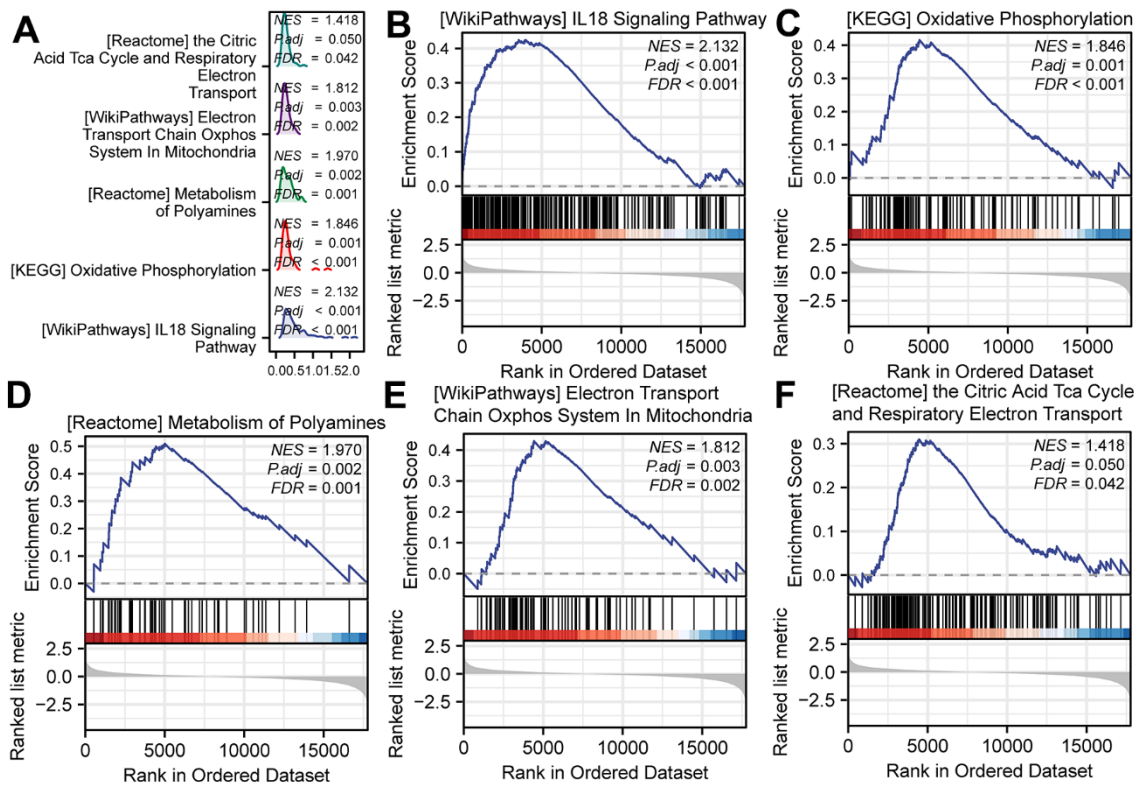
Supplementary Figure 1. Technology roadmap.



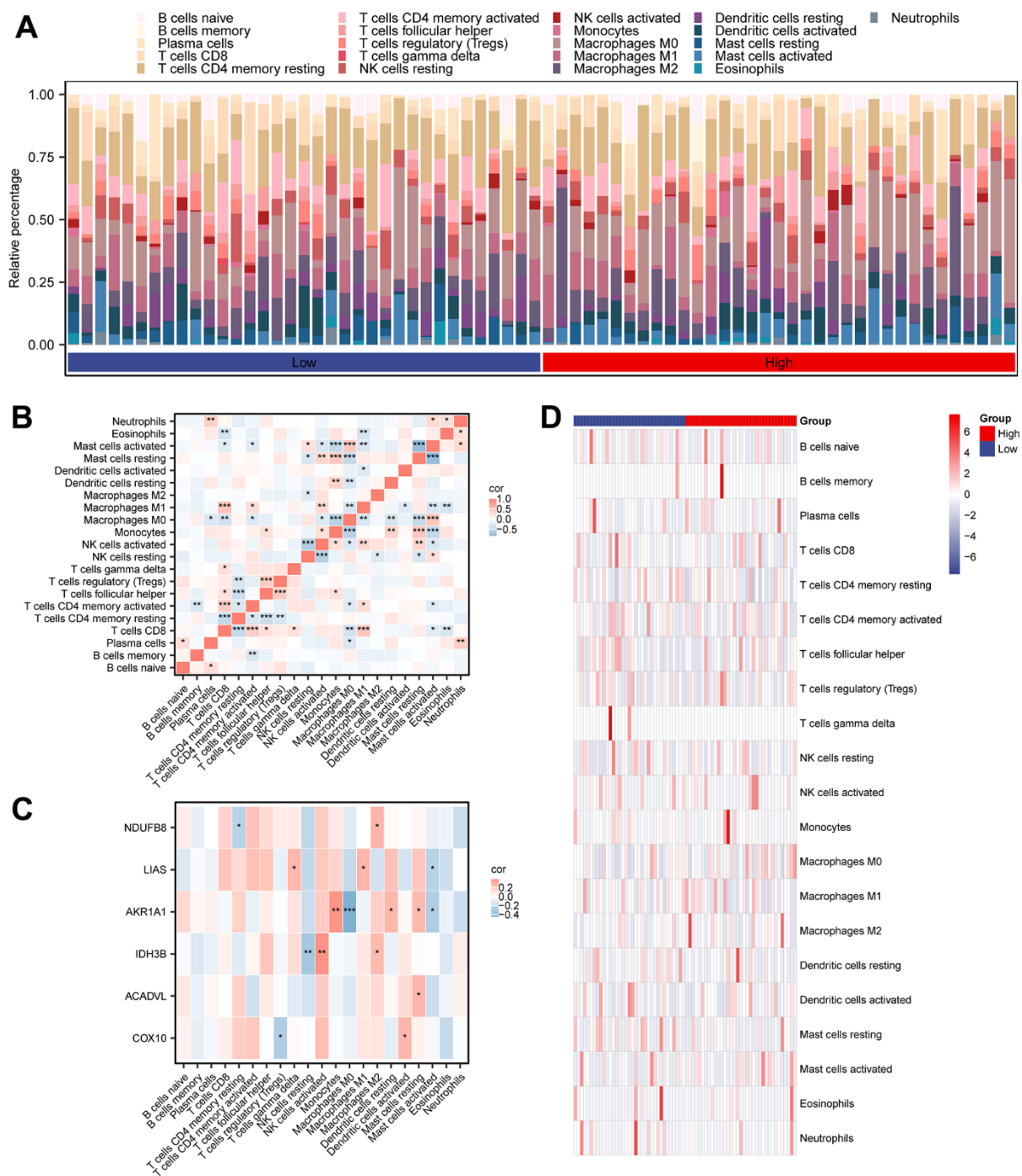
Supplementary Figure 2. Clinical correlation analysis of mitochondrial energy metabolism score and SNP/CNV analysis of MMRGs. (A–F) Clinical correlation analysis of mitochondrial energy metabolism score with Age (A), Gender (B), T stage (C), N stage (D), M stage (E), and Stage (F). (G) Overall SNP analysis of MMRGs in TCGA-ESCC. (H) Mutation waterfall plot of MMRGs in TCGA-ESCC. (I) CNV analysis of MMRGs in TCGA-ESCC. MMRGs, Mitochondrial metabolism-related genes. SNP, single nucleotide polymorphism. CNV, Copy Number Variation.



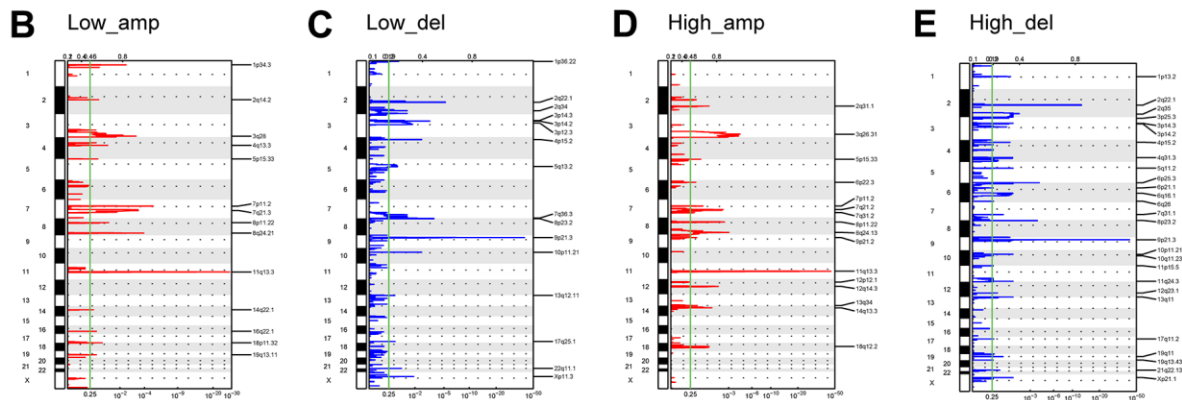
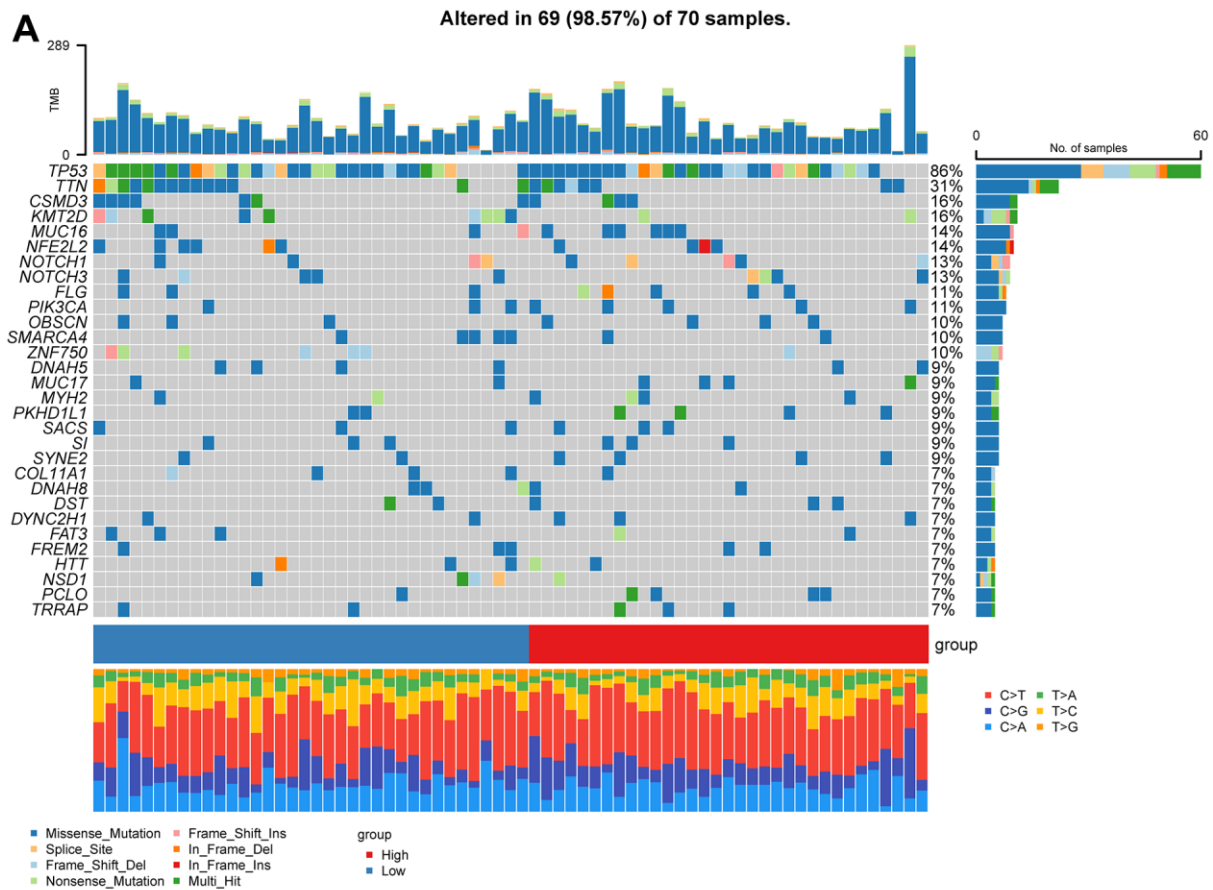
Supplementary Figure 3. Verify set collection and calibrate. (A) The boxplot plot of the merged dataset before removing the batch. (B) The boxplot plot of the merged dataset after removing batches. (C) Merge the PCA plot of the dataset before removing the batch. (D) PCA plot after merging the dataset and removing batches. PCA: Principal Component Analysis.



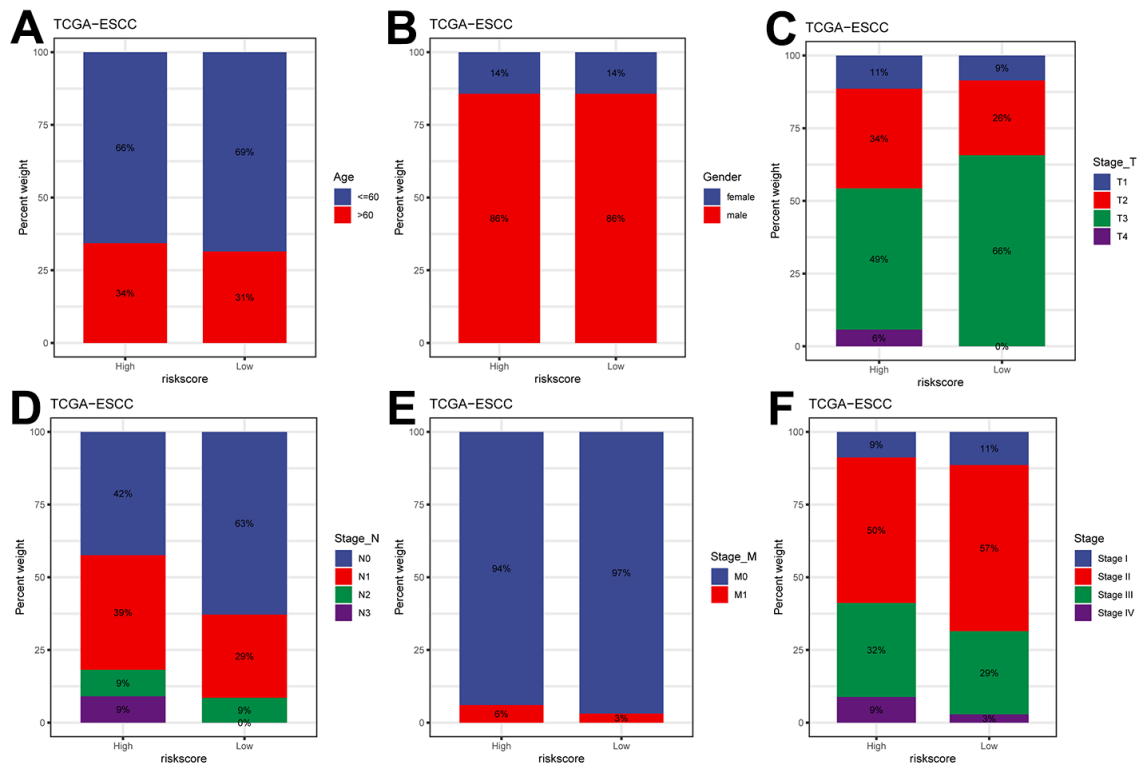
Supplementary Figure 4. The GSEA of the TCGA-ESCC dataset. (A) Volcano plot of the GSEA enrichment analysis of the TCGA-ESCC dataset. (B–F) Pathway maps of the IL 18 Signaling Pathway (B), KEGG Oxidative phosphorylation (C), Metabolism of polyamines (D), Electron transport chain OXPHOS system in mitochondria (E), and Electron Transport (F) pathways.



Supplementary Figure 5. Immune infiltration analysis of the TCGA-ESCC. (A) Stacked bar chart of immune cell infiltration in the High and Low groups of the TCGA-ESCC. (B) Correlation heatmap of immune cells. (C) Correlation heatmap of immune cells and key genes. (D) Heatmap of immune cell infiltration in the TCGA-ESCC.

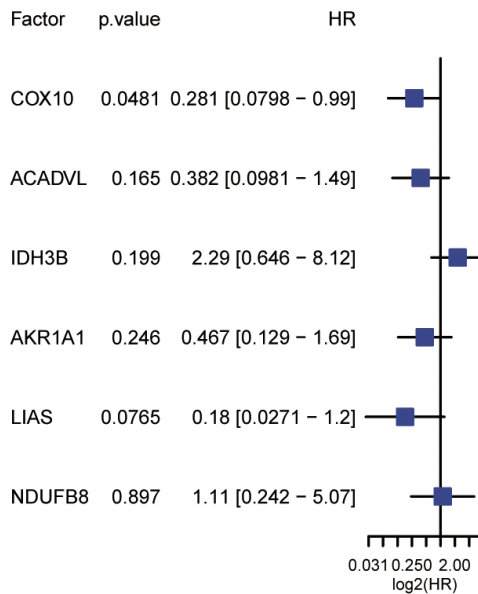


Supplementary Figure 6. SNP and CNV analysis of high-risk and low-risk groups in the Cox model. (A) Waterfall plot of mutation analysis for high- and low-risk groups in the Cox model. **(B, C)** GISTIC analysis of the low-risk group in the TCGA-ESCC dataset. Red indicates CNV amplification **(B)**, while blue denotes CNV deletion **(C)**. **(D, E)** GISTIC analysis of the high-risk group in the TCGA-ESCC dataset. Red represents CNV amplification **(D)**, while blue represents CNV deletion **(E)**.

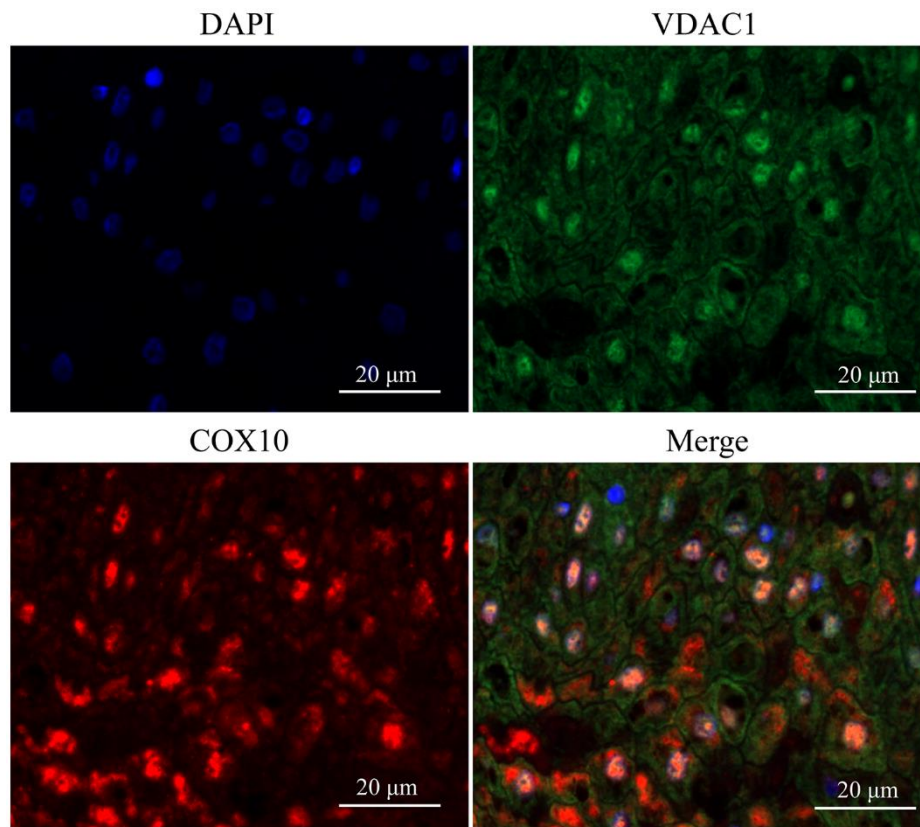


Supplementary Figure 7. Clinical prediction model based on risk score in the TCGA-ESCC dataset. (A–F) Clinical correlation analysis of mitochondrial energy metabolism score with Age (A), Gender (B), T stage (C), N stage (D), M stage (E), and Stage (F).

multifactor Cox regression analysis



Supplementary Figure 8. Risk factor map of MMRGs prognostic model.



Supplementary Figure 9. Immunofluorescence quantitative expression of COX10 in normal oesophageal tissues.

Supplementary Tables

Please browse Full Text version to see the data of Supplementary Tables 3, 6.

Supplementary Table 1. List of MMRGs.

NDUFAB1	ALDH3A1	COX7B	NDUFB8
ALDH3B1	NDUFC1	ACLY	COX11
COX10	PPARGC1A	NDUFA2	IDH3A
MDH1	CPT1A	PPARG	ACAA2
COX15	PDHX	ALDH3B2	NDUFV1
NDUFS1	ALDH2	COX5B	ECI1
ALDH18A1	GAPDH	NDUFB5	PDHB
ACAA1	PPARD	ALDH1B1	ACOX2
CS	ALDH5A1	HADHB	UQCRFS1
NDUFB4	EHHADH	IDH1	PFKFB3
PFKP	PFKFB4	PPA2	NDUFA3
IDH3G	NDUFS7	HADH	BPGM
ACSL4	ACADL	NDUFA9	ADH6
ALDH3A2	PDC	ETFPA	PC
ACADVL	ACADM	PFKL	PAAF1
SDHA	SDHB	ALDH9A1	NDUFV2
ACAT1	HMGCL	SDHC	COX5A
ATP12A	AKR1A1	PKLR	CYC1
OXCT1	ALDH8A1	ALDH1L1	PPA1
HADHA	NDUFB3	NDUFS6	NDUFB1
ACOX3	NDUFA8	MDH2	ALDH1A3
NDUFB2	DLST	NDUFB11	NDUFA6
DLD	ALDH6A1	DLAT	ATP4B
NDUFB7	ACAT2	ACSL1	NDUFA13
ACO2	LIAS	PFKM	PPARA
NFATC4	ACO1	CYP2U1	CYP4A11
IDH3B	ACADS	CPT2	ADH1A
ACSBG1	PFKFB2	PFKFB1	NDUFA4
GPI	ACSL3	NDUFS2	ACADSB
GCDH	NDUFA1	ADPGK	ADH1B
ATP4A	COX7C	ALDH4A1	ACSL5
GAPDHS	ECHS1	ACOX1	HTT
OGDH	POR	NDUFS4	ECI2
AHR	PPAT	ACSL6	OXCT2
GCK	NDUFA5	ALDH7A1	SDHD
MINPP1	ALDH1A2	COX6C	NDUFS3
LHPP	ACSBG2	ALDH1A1	ADH1C
C1QBP	NDUFA10	NDUFB6	NDUFA7

Supplementary Table 2. The details of antibodies.

Name	Catalog No.	Company
ACADVL	14527-1-AP	Proteintech
COX10	10611-2-AP	Proteintech
IDH3B	K006914P	Solarbio
AKR1A1	15054-1-AP	Proteintech
LIAS	11577-1-AP	Proteintech
NDUFB8	14794-1-AP	Proteintech
VDAV1	GB111939	Servicebio

Supplementary Table 3. List of MEtan and MEblue related genes.**Supplementary Table 4. GO and KEGG enrichment analysis results of MEtan related genes.**

ONTOLOGY	ID	Description	GeneRatio	BgRatio	p-value	p.adjust	q-value
BP	GO:0050891	multicellular organismal water homeostasis	7/151	59/18800	4.51E-07	0.000673378	0.000648524
BP	GO:0030104	water homeostasis	7/151	66/18800	9.82E-07	0.000733374	0.000706306
CC	GO:0045177	apical part of cell	16/158	424/19594	3.47E-07	6.45E-05	6.06E-05
CC	GO:0016324	apical plasma membrane	14/158	358/19594	1.28E-06	0.000118886	0.000111687
MF	GO:0004867	serine-type endopeptidase inhibitor activity	7/154	98/18410	1.83E-05	0.004830767	0.004301305
MF	GO:0005506	iron ion binding	8/154	151/18410	4.04E-05	0.004830767	0.004301305
MF	GO:0070330	aromatase activity	4/154	25/18410	5.19E-05	0.004830767	0.004301305
MF	GO:0004866	endopeptidase inhibitor activity	8/154	180/18410	0.00013859	0.007255809	0.006460558
MF	GO:0061134	peptidase regulator activity	9/154	230/18410	0.000139868	0.007255809	0.006460558
MF	GO:0030414	peptidase inhibitor activity	8/154	187/18410	0.00018012	0.007255809	0.006460558
MF	GO:0008236	serine-type peptidase activity	8/154	191/18410	0.000208121	0.007255809	0.006460558
MF	GO:0061135	endopeptidase regulator activity	8/154	194/18410	0.000231388	0.007255809	0.006460558
MF	GO:0017171	serine hydrolase activity	8/154	195/18410	0.000239602	0.007255809	0.006460558
MF	GO:0046906	tetrapyrrole binding	7/154	149/18410	0.000260065	0.007255809	0.006460558
MF	GO:0016712	oxidoreductase activity, acting on paired donors, with incorporation or reduction of molecular oxygen, reduced flavin or flavoprotein as one donor, and incorporation of one atom of oxygen	4/154	40/18410	0.000340417	0.008634215	0.007687888

Supplementary Table 5. GO and KEGG enrichment analysis results of MEblue related genes.

ONTOLOGY	ID	Description	GeneRatio	BgRatio	p-value	p.adjust	q-value
BP	GO:0030198	extracellular matrix organization	108/815	307/18800	3.43E-69	1.20E-65	9.18E-66
BP	GO:0043062	extracellular structure organization	108/815	308/18800	5.09E-69	1.20E-65	9.18E-66
BP	GO:0045229	external encapsulating structure organization	108/815	310/18800	1.11E-68	1.74E-65	1.34E-65
BP	GO:0031589	cell-substrate adhesion	76/815	364/18800	4.09E-31	4.81E-28	3.69E-28
CC	GO:0062023	collagen-containing extracellular matrix	129/839	429/19594	7.25E-74	3.15E-71	2.54E-71
CC	GO:0005788	endoplasmic reticulum lumen	74/839	311/19594	1.30E-34	2.84E-32	2.28E-32
CC	GO:0005604	basement membrane	35/839	95/19594	6.68E-24	9.68E-22	7.80E-22
CC	GO:0005581	collagen trimer	32/839	86/19594	4.04E-22	4.40E-20	3.54E-20
MF	GO:0005201	extracellular matrix structural constituent	73/803	172/18410	1.88E-53	1.36E-50	1.19E-50
MF	GO:0005178	integrin binding	52/803	156/18410	4.58E-32	1.66E-29	1.45E-29
MF	GO:0005518	collagen binding	35/803	68/18410	8.37E-30	2.02E-27	1.77E-27
MF	GO:0030020	extracellular matrix structural constituent conferring tensile strength	23/803	41/18410	3.64E-21	6.59E-19	5.78E-19
KEGG	hsa04510	Focal adhesion	46/345	201/8164	5.90E-22	1.65E-19	1.37E-19
KEGG	hsa04512	ECM-receptor interaction	29/345	88/8164	6.99E-19	9.78E-17	8.13E-17
KEGG	hsa04151	PI3K-Akt signaling pathway	50/345	354/8164	1.81E-14	1.69E-12	1.41E-12
KEGG	hsa04974	Protein digestion and absorption	26/345	103/8164	6.46E-14	4.52E-12	3.76E-12

Supplementary Table 6. DEGs of Cox Multifactorial Model.

Supplementary Table 7. GO and KEGG enrichment analysis results of DEGs.

ONTOLOGY	ID	Description	GeneRatio	BgRatio	p-value	p.adjust	q-value
BP	GO:0035082	axoneme assembly	9/337	87/18800	2.58E-05	0.041122402	0.038946937
BP	GO:0051321	meiotic cell cycle	16/337	266/18800	2.64E-05	0.041122402	0.038946937
CC	GO:0097060	synaptic membrane	19/365	373/19594	8.01E-05	0.019777997	0.017487913
CC	GO:0099699	integral component of synaptic membrane	11/365	149/19594	0.000112495	0.019777997	0.017487913
CC	GO:0005581	collagen trimer	8/365	86/19594	0.000201205	0.019777997	0.017487913
CC	GO:0099240	intrinsic component of synaptic membrane	11/365	160/19594	0.000210965	0.019777997	0.017487913
CC	GO:0062023	collagen-containing extracellular matrix	19/365	429/19594	0.000472793	0.035459497	0.03135366
CC	GO:0043025	neuronal cell body	20/365	482/19594	0.000765607	0.042886688	0.037920861
CC	GO:0043186	P granule	4/365	25/19594	0.001099257	0.042886688	0.037920861
CC	GO:0045495	pole plasm	4/365	25/19594	0.001099257	0.042886688	0.037920861
CC	GO:0060293	germ plasm	4/365	25/19594	0.001099257	0.042886688	0.037920861
CC	GO:0033391	chromatoid body	3/365	12/19594	0.001244723	0.042886688	0.037920861
CC	GO:0043679	axon terminus	8/365	113/19594	0.00125801	0.042886688	0.037920861
CC	GO:0042734	presynaptic membrane	9/365	143/19594	0.001462779	0.044367549	0.039230254
CC	GO:0099056	integral component of presynaptic membrane	6/365	67/19594	0.001538075	0.044367549	0.039230254
KEGG	hsa04080	Neuroactive ligand-receptor interaction	18/157	362/8164	0.000192278	0.044800794	0.043717964

Supplementary Table 8. GSEA analysis of TCGA-ESCC.

ID	setSize	enrichmentScore	NES	p-value	p.adjust	q-value
WP_IL18_SIGNALING_PATHWAY	266	0.424215445	2.132058722	1.00E-10	1.92E-08	1.61E-08
KEGG_OXIDATIVE_PHOSPHORYLATION	113	0.415750078	1.845639559	2.60E-05	0.001010257	0.000848607
REACTOME_METABOLISM_OF_POLYAMINES	58	0.509149923	1.970004759	4.99E-05	0.001612593	0.001354564
WP_ELECTRON_TRANSPORT_CHAIN_OXPPOS_SYSTEM_IN_MITOCHONDRIA	89	0.42884856	1.811634293	0.000100966	0.002762688	0.002320634
REACTOME_THE_CITRIC_ACID_TCA_CYCLE_AND_RESPIRATORY_ELECTRON_TRANSPORT	165	0.310160102	1.417800478	0.00436255	0.049829122	0.041856042
REACTOME_EUKARYOTIC_TRANSLATION_ELONGATION	93	0.655696748	2.794520902	1.00E-10	1.92E-08	1.61E-08
KEGG_RIBOSOME	87	0.652148161	2.753509857	1.00E-10	1.92E-08	1.61E-08
REACTOME_SRP_DEPENDENT_COTRANSLATIONAL_PROTEIN_TARGETING_TO_MEMBRANE	113	0.615279554	2.731410875	1.00E-10	1.92E-08	1.61E-08
REACTOME_EUKARYOTIC_TRANSLATION_INITIATION	120	0.617030923	2.716149663	1.00E-10	1.92E-08	1.61E-08
REACTOME_RESPONSE_OF EIF2AK4_GCN2_TO_AMINO_ACID_DEFICIENCY	102	0.589136754	2.558808696	1.00E-10	1.92E-08	1.61E-08
REACTOME_SIGNALING_BY_THE_B_CELL_RECEPTOR_BCR	109	0.565117207	2.533317502	1.00E-10	1.92E-08	1.61E-08
REACTOME_NONSENSE_MEDIATED_DECAY_NMD	116	0.549081018	2.438119496	1.00E-10	1.92E-08	1.61E-08
REACTOME_REGULATION_OF_EXPRESSION_OF_SLITS_AND_ROBOS	171	0.503232522	2.306612557	1.00E-10	1.92E-08	1.61E-08
REACTOME_OLFACTORY_SIGNALING_PATHWAY	98	-0.695478407	-2.251386071	1.00E-10	1.92E-08	1.61E-08
KEGG_OLFACTORY_TRANSDUCTION	115	-0.679815158	-2.228880628	1.00E-10	1.92E-08	1.61E-08

Supplementary Table 9. List of miRNAs related key genes.

mRNA	miRNA
COX10	hsa-miR-4533
COX10	hsa-let-7c-3p
COX10	hsa-miR-6809-3p
COX10	hsa-miR-765
COX10	hsa-miR-6124
COX10	hsa-miR-7110-5p
COX10	hsa-miR-5681b
COX10	hsa-miR-11181-3p
COX10	hsa-miR-1343-5p
COX10	hsa-miR-939-5p
COX10	hsa-miR-4492
ACADVL	hsa-miR-5582-5p
ACADVL	hsa-miR-302e
ACADVL	hsa-miR-124-3p
ACADVL	hsa-miR-506-3p
IDH3B	hsa-miR-4447
IDH3B	hsa-miR-4472
IDH3B	hsa-miR-4533
IDH3B	hsa-miR-324-3p
LIAS	hsa-miR-335-3p
LIAS	hsa-miR-3913-5p
LIAS	hsa-miR-3122
LIAS	hsa-miR-1302
LIAS	hsa-miR-4635
LIAS	hsa-miR-2114-5p
LIAS	hsa-miR-892c-5p
LIAS	hsa-miR-493-3p
LIAS	hsa-miR-4503
LIAS	hsa-miR-4298
LIAS	hsa-miR-5010-3p
LIAS	hsa-let-7g-3p
LIAS	hsa-let-7a-2-3p
LIAS	hsa-miR-4679
LIAS	hsa-miR-548b-3p
NDUFB8	hsa-miR-4682
NDUFB8	hsa-miR-513c-3p
NDUFB8	hsa-miR-513a-3p
NDUFB8	hsa-miR-3606-3p